Summer 2024

Processing & Properties of Zirconium Carbide Manufactured by Ceramic On-Demand Extrusion

Clare Sabata
Missouri University of Science and Technology

Department:

PROCESSING & PROPERTIES OF ZIRCONIUM CARBIDE MANUFACTURED BY CERAMIC ON-DEMAND EXTRUSION

by

CLARE CATHERINE SABATA

A THESIS

Presented to the Graduate Faculty of the

MISSOURI UNIVERSITY OF SCIENCE AND TECHNOLOGY

In Partial Fulfillment of the Requirements for the Degree

MASTER OF SCIENCE

in

CERAMIC ENGINEERING

2024

Approved by:

Gregory E. Hilmas, Advisor
Jeremy L. Watts
Ming C. Leu

PUBLICATION THESIS OPTION

This thesis consists of the following two manuscripts, which have been or will be submitted for publication:

Paper I, found on pages 29-53, entitled “Development of a highly loaded zirconium carbide paste for material extrusion additive manufacturing”, has been submitted to the *Journal of Additive Manufacturing*.

Paper II, found on pages 54–78, entitled “Thermal and mechanical properties of zirconium carbide manufactured via ceramic on-demand extrusion”, is being drafted for publication.

ABSTRACT

This research focuses on the development of a zirconium carbide (ZrC) paste for use in material extrusion direct ink write additive manufacturing (AM) followed by the pressureless densification of ZrC and the mechanical and thermal characterization of the resulting ceramics. A highly loaded, aqueous paste was developed using commercial ZrC powder ball milled to ~1 μm. Optimal dispersant, binder, and solids loading were found by rheological characterization. The paste composition consisted of 46-47 vol% ZrC, 43.5 vol% distilled water, 8.1 vol% dispersant, and 1.6 vol% binder. A yield stress of ~8 Pa allowed for shape retention upon removal of shear. Thermogravimetric analysis was employed to build a debinding schedule. A pressureless sintering schedule of 2000°C for 2 hours in He atmosphere produced ZrC greater than 90% density with grains <5 μm. ZrC test samples were printed, debinded, and sintered. X-ray diffraction confirmed ZrC was the only phase present in printed parts. Four-point flexural testing demonstrated an average strength of 331.3 ± 57.1 MPa with a Young's modulus of 232.8 ± 13.1 GPa. Vickers microhardness was 13.6 ± 1.0 GPa at a load of 4.91 N and 11.6 ± 0.5 GPa at a load of 9.81 N. Fracture toughness was 2.9 ± 0.2 MPa·$m^{1/2}$. The largest grain was the critical flaw as determined by Griffith analysis. Thermal conductivity generally increased with temperature from 13.4 W/m·K at room temperature to 27.1 W/m·K at 2000°C. Room temperature electrical resistivity was found to be 122.4 ± 0.5 μΩ·cm; the electron contribution to thermal conductivity was 29% and the phonon contribution was 71%. The developed paste and characterized material add a new method of AM to the processing of ZrC.

ACKNOWLEDGMENTS

I would like to thank my advisor, Dr. Gregory Hilmas, for his guidance, advice, and support throughout my graduate career. Next, I would like to thank Dr. Jeremy Watts for his guidance and assistance in the laboratory. Finally, I want to thank Dr. Ming Leu for his support in the additive manufacturing space.

I want to send a huge thank you to my peers in the ultra-high temperature ceramics group in McNutt 307. They taught me how to use the equipment and provided guidance during data analysis. I appreciate their support during my graduate studies.

Lastly, I want to thank my family for their support and love. I could not have gotten here without you. I want to especially thank my husband, Jon Voss, for his undying love, understanding, and patience throughout these past two years. I appreciate all of you for always believing in me.

TABLE OF CONTENTS

LIST OF ILLUSTRATIONS

SECTION Page

LIST OF TABLES

PAPER I Page

NOMENCLATURE

Symbol	Description
τ	Applied Shear Stress
τ_0	Yield Stress
n	Flow Behavior Index
K	Consistency Coefficient
η	Viscosity
ϕ_{SDS}	Amount of Dispersant
G’	Elastic Behavior
G"	Viscous Behavior
h_{max}	Maximum Layer Height
σ_y^{Dyn}	Yield Stress
ρ	Density
g	Gravity
$\sigma_{y,critical}$	Critical Yield Stress
S	Strength
P	Load
L	Support Span
b	Specimen Width
d	Specimen Thickness
HV	Vickers Hardness
K_{1c}	Fracture Toughness

E	Elastic Modulus
H	Hardness
c	Crack Length
a	Critical Flaw Size
Y	Geometric Shape Factor
σ	Strength
k	Thermal Conductivity
d	Diffusivity
C_p	Heat Capacity
k_e	Electron Contribution to Thermal Conductivity
σ	Electrical Conductivity
L_0	Lorenz Number
T	Temperature
k_p	Phonon Contribution to Thermal Conductivity
k, a, b	Empirical Constants
G	Grain Size
P	Volume Fraction Porosity
E_0	Modulus Adjusted for Porosity
ρ	Porosity Shape Factor
$H_v(0)$	Hardness Adjusted for Porosity
k_{por}	Thermal Conductivity Adjusted for Porosity
σ_{th}	Electrical Conductivity Adjusted for Porosity

1. INTRODUCTION

Ultra-high temperature ceramics are defined as ceramics that have melting points of over 3000°C[1, 2]. They typically have properties that make them candidates for use in extreme environments, due to the combination of metallic and ceramic character. One of these materials, zirconium carbide (ZrC), has a high melting point of ~3500°C, hardness of 20-30 GPa, modulus of ~400 GPa, low density of 6.73 g/cm^3, and high wear resistance[3–5]. Typical densification of ZrC requires high temperatures (>2000°C) and pressures (30-100 MPa)[6–9] that can be accomplished with hot pressing and spark plasma sintering. However, this limits the ceramic geometry that can be prepared, as subjecting green bodies with complex shapes to high pressures will collapse the desired shape. Pressureless sintering of ZrC can be successful, but often requires reducing surface oxides, reducing particle size, and/or adding sintering aids[10–12]. Green machining, while viable, is not standardized[13]; post-sintering machining is costly and often requires diamond tooling[14].

Additive manufacturing (AM) has recently gained interest in the ceramic field as a new processing method to form complex geometries at a reduced machining cost[14]. The AM of ZrC has been reported by the methods of selective laser sintering[15] and binder jetting[16]. These methods produced ceramics that had thermal stresses and high porosity, respectively. It was desired to add another method of AM to the processing of ZrC, namely material extrusion by direct ink write (DIW). DIW deposits pastes layer wise to build a part. In this work, the desired method of DIW is known as ceramic on-demand extrusion (CODE). CODE employs an auger for enhanced start/stop control of the paste during deposition, is performed at room temperature, and can print large parts (tens of

centimeters)[17, 18]. The current material palette of CODE includes zirconia[19], alumina[18], silicon nitride[20], and functionally graded materials[21]. CODE depends on the rheological behavior of the ceramic paste to hold its shape post-deposition[22].

The goals of this work include developing a ZrC paste that could be used to repeatably additively manufacture ZrC ceramics combined with an effective pressureless sintering schedule to obtain densities >90%, followed by characterization of several mechanical and thermal properties of ZrC produced by CODE to compare to traditionally processed ZrC. Understanding the behavior of both the developed paste and sintered ceramic will add another material system to the CODE material palette.

2. LITERATURE REVIEW

2.1. CURRENT STATE OF CERAMIC ADDITIVE MANUFACTURING

Commercial use of additive manufacturing (AM) began in 1987 using the stereolithography method[23]. Interest in AM picked up in the 90's and 2000's but was typically reserved for use in the polymer and metal fields[23]. Since then, many methods of AM have been developed and shown to be effective for ceramic manufacturing, including three-dimensional printing (3DP), selective laser sintering (SLS), stereolithography (SLA), laminated object manufacturing (LOM), and 3D extrusion freeforming (EFF). Machining of ceramic materials is costly and time consuming, typically accounting for 80% of final part expenses as diamond tooling is often required for ceramic machining[13, 14]. For this reason, additive manufacturing (AM) is an attractive method of ceramic production for researchers and industry alike as well as the ability to produce geometrically complex parts that would be impossible using traditional processing means. Travitzky et al. published a comprehensive review over these methods as they relate to ceramic materials[14].

2.1.1. 3D Printing Direct 3DP is a method of AM that deposits a well-dispersed ceramic suspension to build a part, while indirect 3DP may be better known as binder jetting, in which binder is ejected onto a ceramic powder bed layer by layer to build a part[14]. In binder jetting, a thin layer of powder is spread across the build platform, at which point the printer deposits binder according to a shape file to join the powder particles together. The build platform is lowered, a fresh layer of powder is spread, and the process repeats until the part is printed. 3DP has been used to manufacture structural,

orthopedic, electronic, dental, and optical materials[24]. The density of the powder bed is related to the final density of the printed part, where high particle packing due to particle morphology and size distribution in the powder bed leads to a higher green density[25]. Also, the use of a powder bed allows for large overhangs and lattice structures to be printed without the need for extra support material[26], but high porosity is often observed in printed parts[27].

Özkol used direct 3DP to produce dental implants using a 3Y-TZP ink that had good shape fidelity[28]. Much of that work was based on characterizing the inks to be used in the direct 3DP process. They found that the ceramic particles will not clog a nozzle if the nozzle diameter is about 30 times the size of the d_{90} value of the powder. Rheological characterization of the inks showed what viscosities, surface tensions, particle size distributions, zeta potential, and inverse Ohnesorge numbers (drop formation behavior) were applicable to this method. In fact, the authors state that this method is applicable to many ceramic systems demonstrating a range of behaviors. Final printed parts, using inks of 22 and 27 vol%, had relative green densities of 50% and sintered densities of 97%, with no major defects.

Mott and Evans utilized direct 3DP to additively manufacture functionally graded zirconia/alumina ceramics having a small step height and a gradient that followed the modeled gradient[29]. However, the sintering of the alumina portion of the composite was restricted to 70% relative density. The only way to increase the densification of the alumina was to remove the zirconia portion before sintering. The composites also experienced warping during sintering and large pores that could be attributed to printing defects.

Metal matrix composites were investigated using the indirect 3DP (binder jetting) technique by Snelling et al[30]. A cellular-lattice structure was printed from cordierite to be infiltrated with a zinc alloy post-sintering. The ceramic sintered to 92% relative density, but final three-point bend strength, modulus, and toughness values for the MMC were lower than the constituent materials. The authors believe this to be due to the lack of mechanical/chemical interfacial bonding between the ceramic and the metal as well as defects in the ceramic due to the printing process.

Mariani et al. utilized binder jetting to manufacture alumina ceramics[31]. The powder used had a d_{50} value of 9 μm, and they attributed this fine particle size to the ability to print parts with greater than 60% relative green density. The final sintered parts had a relative density of 75%, with a three-point flexural strength of 56.1 MPa and Vickers hardness of 1.95 GPa. The authors note the importance of the powder bed packing and flowability of the material, control of both of which is essential to the success of a printed part[32].

2.1.2. Selective Laser Sintering Direct SLS uses a high-power laser to locally sinter powder together followed by the spreading of more powder on top to build a part layer wise; the sintering of powder during printing prevents the need for a post-printing sinter step[14]. Indirect SLS bonds low temperature phases, such as binders, on the ceramic powders together. Therefore, indirect SLS requires post-processing steps to debind the green part as well as densify to the final ceramic. Important characteristics of this technique include particle size/powder flowability and laser parameters, where larger particles and spherical shapes promote better flowability. The type of laser and corresponding wavelength are chosen based on the absorption of the powder to be

sintered; the scanning speed, laser power, and spot size can all be adjusted to suit the material system[33]. Currently, CO_2 and Nd:YAG lasers are popular for ceramic SLS.

Slocombe and Li showed that SLS can be used to produce TiC-Al_2O_3 composites by utilizing the laser to induce the self-propagating high temperature synthesis (SHS) reaction between TiO_2, Al, and C[34]. Laser parameters were determined and found to be 60 W, 20 kHz frequency, with a scan speed of 2 mm/s. The goal of this work was to determine the laser parameters that may be used to react constituent powders into the desired composite. Ahmed et al. expanded on this work, using the SHS reaction and SLS method to simultaneously process and densify TiC-Al_2O_3 composites[35]. The authors report a minimum open porosity of 7 vol%, a maximum Vickers hardness of 6.35 GPa, and fracture toughness of 3.5 $MPa \cdot m^{1/2}$.

Friedel et al.[36] used SLS to prepare SiOC-SiC ceramics by using a pre-ceramic polymer that was locally cured by the laser. Post-printing, the part was converted to SiOC-SiC and infiltrated with liquid silicon to achieve dense parts with a bending strength of 220 MPa. This work focused on varying laser parameters and how it affected the final sample. They found that when laser power is too high, the polymer would burn and waste ceramic. Conversely, a laser power that is too low would not melt the polymer at all. The researchers were successful in manufacturing geometrically complex samples, including a turbine wheel.

Pure yttria-zirconia powders were sintered via SLS[37]. Bertrand et al. utilized direct SLS to manufacture zirconia ceramics. They found that while the final density and mechanical properties of prepared samples did not meet the desired criteria, this method was able to produce zirconia without using a secondary binder phase. The authors

mention that the density of the powder bed is the limiting factor to overall densification of the final part. But, because the part was sintered as it was built, the need for a post-printing sintering step was unnecessary. Geometries of printed parts closely matched the modeled object, although the surface texture was quite rough.

SLS can also be used with a slurry instead of a powder bed. Ceramic powders tend to not flow well due to morphology and size. Waetjen et al. deposited ceramic slurries via an airbrush which was then SLS'd to print samples[38]. Alumina and zirconia slurries were developed, and varying laser powers were utilized to find what parameters promoted densification versus drying of the slurry. Alumina samples achieved 98.5% relative density while zirconia reached 98% relative density. However, the authors mention that while individual zirconia layers achieved high density, the lack of a glassy phase prevented the formation of an entirely dense structure.

While the above examples demonstrate successes in ceramic SLS, this method is only typically used when a lower temperature liquid phase is present to achieve highly dense ceramics due to the elevated temperatures often necessary to process ceramics. The short duration of the laser scanning can also lead to thermal gradients and residual stresses, which may cause cracking[33]. For this reason, metal and polymer SLS has been more commercialized as compared to ceramic SLS[14, 39].

2.1.3. Stereolithography SLA employs a UV-curable resin loaded with ceramic particles that is cured layer by layer until the final part is constructed. A vat of ceramic loaded photopolymerizable medium is prepared, then a laser is used to scan the design of the part to polymerize the resin. The build platform is dropped down, more resin is spread on top of the previous layer, and the next layer is scanned[40]. A post-printing heat

treatment is then used to pyrolyze the polymer to obtain the green part[14]. Green density of formed parts is related to the solids loading of the resin; to achieve acceptable densification, the resin must be 50 vol% solids or higher[40]. The remaining volume fraction of the resin is the polymer itself, which leads to sometimes long and challenging debinding steps. Rheological behavior of the resin is necessary to control. The shear forces experienced by the resin depend on the resin being spread on deep liquid or on top of a solid layer. Along with this, the suspension must be stable enough to prevent the particles from settling. It is also recommended to use ceramic particles that to not absorb light in the UV spectrum, as this will prevent the resin from polymerizing; the refractive index of the powder should also be only slightly different from the refractive index of the resin of choice. Therefore, much of the research on ceramic SLA has been performed on alumina, zirconia, silica, hydroxyapatite, zirconate titanate oxides, and silicon nitride[41]. This principle has been used as far back as 1986, when Lee et al. developed photopolymerizable binders for ceramics for production of ceramic substrates[42].

Chartier et al.[43] developed a highly loaded (up to 60 vol%) resin for use in SLA, and were able to print alumina, zircon, and silica. Various alumina particle sizes were studied to determine the effect of particle size and all three powders were compared as a function of refractive index. The authors found that cure depth follows a linear relationship with particle size, while cure depth decreased as a function of refractive index. Alumina samples sintered to 97% relative density. The authors quote an average value of 275 MPa for alumina mechanical characterization, but do not specify the measured mechanical property.

The effect of plasticizer on the properties of alumina prepared by SLA was explored by Xing et al[44]. Suspensions of 48 vol% alumina were prepared with 20 to 28 wt% plasticizer. The goal of the work was to determine the amount of plasticizer necessary to prevent delamination of green bodies post-printing. Plasticizer content was determined by the highest amount of plasticizer that decreased delamination that also does not introduce flaws into the interface of two layers. A maximum density of 99.01% and a three-point flexural strength of 486 MPa was achieved. This work increased the strength of green bodies which led to final densities and strengths that are comparable to traditionally processed alumina.

Integrally cored ceramic molds fabricated of silica were manufactured by SLA[45]. The photopolymerizable suspension consisted of 60 vol% fused silica and 1,6 hexanediol diacrylate. Traditionally fabricated cored ceramic molds consist of several steps to fabricate the shell and core, which are then combined to the final part. This work prepared a geometrically complex mold that could be prepared in one step. The final mold had a surface roughness of about 60 μm without delamination between layers. Dimensional accuracy was under 1%. However, the finest features of the mold were not visible in the green or sintered ceramic; the authors attribute this to the large focal point on the laser in comparison to the fine features. The work shows promise for ceramic SLA to take the place of traditional ceramic mold processing.

As for electrical ceramics, Buerkle et al. utilized ceramic SLA to process alumina dielectric antenna arrays[46]. Electrical property measurements verify that the SLA produced array behaves similarly to traditionally produced arrays. The authors also note the advantage of being able to scale the size of the array from a four-by-four

configuration to an eight-by-eight configuration, which is not as simple in the traditional process. Brakora et al. manufactured all-dielectric low-loss microwave components out of alumina by ceramic SLA[47]. The authors state that, generally, ceramics perform better in these applications as compared to metals, but due to difficulty in machining ceramics have not been widely used. They demonstrate the ability to manufacture the first monolithic and ceramic Luneberg lens; this lens is a symmetrical sphere with a dielectric constant that decreases outwards, whose production by traditional routes presents a challenge.

2.1.4. Laminated Object Manufacturing LOM is a unique method of AM as it utilizes planes or sheets of material to build a part. In the case of ceramics, the material is tape cast and then cut to desired shape and laminated layer by layer. A roller of ceramic tape is fed along a table. Once the uncut tape is on the build platform, it is cut by a laser into the shape of the desired layer. The layer can be laminated onto the previous layers either before or after laser cutting, and the build platform drops. The cut tape is rolled onto a waste roll and the process is repeated[48]. One advantage of LOM as compared to other ceramic AM methods is the ability to produce layered structures, although surface quality tends to be low, and highly complex parts (such as undercuts or hollow areas) are not typically feasible with this process[14].

Silicon nitride ceramics were prepared by LOM. Rodrigues et al. used traditional tape casting techniques to prepare the silicon nitride tapes, which were then laminated and cut into the desired shape. For this work, the laser power, cutting speed, roller temperature, and roller speed were controlled to prepare green bodies with the desired shape. The green bodies were debinded and sintered to 97% density. Mechanical

properties of the samples prepared via LOM were measured; Young's modulus of 307 GPa and four-point flexural strength of 918 MPa were comparable to silicon nitride ceramics processed using conventional routes. In comparison, LOM silicon nitride samples studied by Liu et al. displayed a density of 93.7% and three-point bending flexural strength was 475 MPa[49].

Dense (97.1%) alumina was also successfully prepared by LOM [50]. Tapes of thickness 0.7 mm were cast, and samples were printed by LOM. Three-point bend strength was non-uniform depending on how the load was applied to the sample. When the load was parallel to the layers, the strength of the LOM alumina was 145 MPa; conversely, load applied perpendicularly to the layers led to a strength of 228 MPa. The authors attribute this to the interfacial bonding between the layers. While these values did not correspond to conventionally processed alumina, the ability to manufacture alumina by LOM was proven.

The production of glass ceramics of lithia-zirconia-silica-alumina (LZSA) composition by LOM was studied by Gomes et al[51]. Zeta-potential of the powder was measured to optimize the rheological behavior of the suspension. A maximum solids loading of 27 vol% was used. To represent the geometrical complexity of the shapes able to be printed via LOM, a gear wheel was printed using cast tapes. The gear was debinded, sintered, and crystallized. It was found that higher tensile strengths of tapes corresponded to higher tensile strengths of prepared laminates. The prepared gear wheels presented no major defects.

The production of porous alumina was accomplished by freeze-casting LOM[52]. Aqueous-based alumina slurry was tape cast using a doctor blade, and immediately

frozen. The direction of ice crystallization was monitored by cooling rate to control the porosity that will be present in the final part. The desired layer was cut by a laser without melting the ice in the rest of the layer; when the next layer was stacked on the previous, the ice on the surface melts and recrystallizes while in contact with the next layer to improve interfacial bonding of the green part. The green body was obtained by freeze drying the stacked layers which was then sintered to the final part. This work introduced a novel method of AM by combining freeze-casting and LOM to manufacture porous ceramics. By solidifying the slurry and layers during LOM, the green strength of the ceramic was increased, reducing deformation risk of the green part.

2.1.5. Extrusion Freeform Fabrication EFF of ceramics extrudes ceramic feedstock through an orifice to build a ceramic structure. This method utilizes a highly loaded ceramic paste/wire/granulate that is extruded layer by layer to build a ceramic structure[14]. Cesarano et al.[53] introduced this technique in the 90's using the robocasting (RC) technique and a highly loaded alumina paste (50-65 vol%) to print dense alumina structures. The researchers identify the necessity of controlling the rheological behavior of the paste, as the paste needs to be able to be extruded through a small orifice but also hold its shape once deposited. There are many subsections of EFF. The major distinction between the subsections is how the ceramic retains shape post-deposition[54]. Three subsections are included in depth. Fused deposition model of ceramics (FDC) uses a ceramic loaded thermoplastic which is heated, extruded, and cooled to retain shape. Freezeform extrusion fabrication (FEF) freezes deposited suspension in the desired shape. Robocasting (RC) depends on the rheological behavior of the paste/ink to hold shape after deposition[14]. Direct ink write (DIW) is a method of RC has many advantages

over the previously outlined methods, including it being fast, performed at ambient temperature, relatively inexpensive, eco-friendly when using an aqueous solvent, and the ability to print many types of ceramic materials.[55]

Ceramic loaded polymer filaments consisting of 50 vol% alumina, 40.9 vol% EVA co-polymer, and 9.1 vol% stearic acid were prepared for FDC by Conzelmann et al[56]. Several types of structures were printed, including cuboids and tetrahedron with varying amounts of infill (0-100%). Samples were printed using a commercially available fused deposition modeling printer. Due to the high amount of organic in the printed specimens, building a slow debinding schedule was essential for this work; even so, the parts with 100% infill exhibited cracking, warping, and voids due to binder decomposition. Lombardi et al. note several issues that are common within this technique, including increased brittleness of the feedstock and increased melting temperature upon aging[57]. Feedstocks must also be highly homogeneous to ensure no density gradients are present in the printed sample.

Aqueous alumina pastes of 50-55 vol% solids content were printed via FEF[58]. Dispersant content, binder content, and pH of the solvent provided control of the printing behavior of the paste, and overhangs were able to be successfully manufactured without the use of support material. Freeze drying allows for higher shape retention than depending on rheology alone and gives the printed part higher green strength. However, final samples only reached 90% of theoretical density. This was attributed to underfilling of the print due to mismatch between extrusion of paste and printing speed. As compared to FDC, FEF uses a relatively low amount organic, which allows for an aggressive debinding step that can be completed in one day or less.

Direct ink writing of alumina has been widely studied[59]. Rueschhoff et al. manufactured alumina by DIW of 98% relative density with a three-point flexural strength of 134-157 MPa[60]. Glymond and Vandeperre reported densities of 98% of magnesia doped alumina and three-point flexural strength 326 MPa[61]. Mamatha et al. hot isostatically pressed DIW alumina for a density of 97% and three-point flexural strength of 256 MPa. These examples are just a few of the work related to DIW of alumina. Other materials to have been successfully manufactured by DIW include zirconia, cement, silicon carbide, and nitrides[62].

Ceramic on-demand (CODE) extrusion is a method of direct ink write additive manufacturing that is capable of manufacturing large (tens of centimeters^3), dense ceramics. Ghazanfari et al.[18] developed this method to additively manufacture paste-based ceramic materials at room temperature using aqueous based pastes. CODE employs an auger extruder for enhanced start/stop control of paste during deposition as well as high flowrate consistency.[17] Paste preparation for CODE begins by combining ceramic powder, distilled water, and dispersant. This slurry is placed on a slow speed (<40 rpm) ball mill to homogenize the slurry without drastically changing particle size. Once completed, binder is added and mixed to fully incorporate the binder into the paste. Rheological characterization of the paste is often employed to verify the consistency and "printability" of pastes. This paste can then be printed via CODE. The three-axis (X, Y, Z) motion subsystem is controlled through G-code commands with high printing accuracy (18 μm/300 mm). The paste is attached to the auger extruder and subjected to air pressure to force the paste into the auger, at which point it is extruded through a nozzle and deposited layer-by-layer to build the part. During the printing process,

kerosene oil is manually deposited around the edges of the part to prevent uneven drying to reduce cracking. After printing, the part is dried, debinded, and sintered.

There are many advantages to CODE, including the ability to print at room temperature, the use of fine particles and highly loaded pastes promote densification during sintering, eco-friendly aqueous based pastes, capability of functionally graded materials, and more.[19] This method has already been proven to successfully print alumina[18], zirconia[19], silicon nitride[20], and functionally graded materials[21]. A ~60 vol% solids alumina paste used with CODE produced parts that were 98.5% relative density with a three-point bend flexural strength of 364 MPa. The zirconia work used a ~50 vol% solids paste to produce 99% dense parts with four-point bend flexural strength of 278 MPa. Silicon nitride was shown to achieve 98.6% density with mechanical properties that were comparable to traditionally processed Si_3N_4. The functionally graded material showed ~1% difference between actual and desired composition. The current goal for CODE is to expand the printable material palette.

2.2. PROPERTIES OF ZIRCONIUM CARBIDE

The following sections outline the structure, bonding, processing, and typical properties of zirconium carbide.

2.2.1. Crystal Structure & Bonding Zirconium carbide (ZrC) is a member of the ultra-high temperature (UHTC) class of materials as it has a melting point of over 3000°C[1]. ZrC is a group IV transition metal carbide with the rock salt, $Fm\bar{3}m$ crystal structure[4, 63] which can be seen in Figure 2.1. It has a lattice parameter $a = b = c = 4.713$

Å. In this structure, the Zr ions form a face-centered cubic lattice with the C ions in the octahedral interstitial positions.

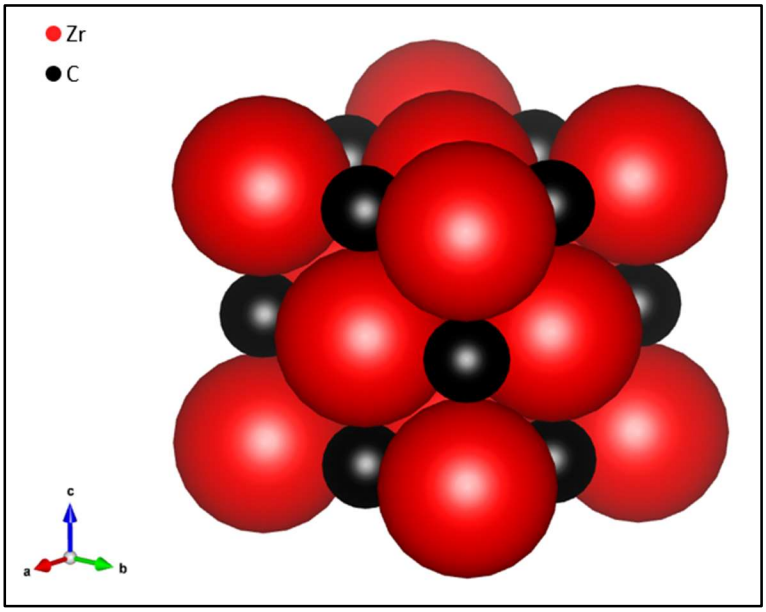

Figure 2.1: Zirconium carbide crystal structure ($Fm\bar{3}m$) visualized using VESTA[66].

However, ZrC tends to be stable over a range of carbon stoichiometries (37.5 – 49.5 atomic% at 1000K), which can be seen in Figure 2.2 as calculated by Guillermet[64]. This range corresponds to up to 50% of carbon sites being unoccupied. Determining the stoichiometry of ZrC is typically done by calculating the Zr/C ratio as a function of lattice parameter as found by x-ray diffraction (XRD) or by inert-gas fusion technique[65]. When the carbon stoichiometry is low, contaminants such as oxygen or nitrogen fill the carbon vacancies.

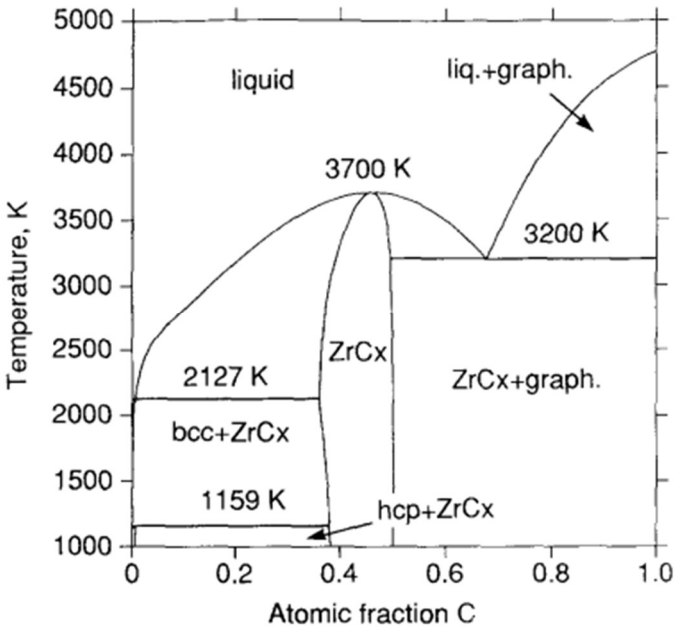

Figure 2.2: Zr-C phase diagram.

ZrC exhibits mixed covalent-metal-ion bonding[67]. The electronic structure of Zr is $[Kr]5s^2 4d^2$ while the structure for carbon is $[He]2s^2 2p^2$. The difference in electronegativity between Zr (1.22) and C (2.50)[68] contributes to ionic bonding. The interaction between the 2p and 4d states of C and Zr, respectively, lead to the covalent bonding present. Finally, the metallic bonding is due to the delocalized electrons that occur when the Zr atoms are ionized. It is because of this strong bonding character that ZrC has a high melting temperature (~3550°C), high hardness (~25 GPa), and Young's modulus (~400 GPa). It also has a relatively low density of 6.73 g/cm^3, especially when compared to its melting temperature. Figure 2.3 shows melting temperature for several high temperature materials. ZrC not only has the third highest melting temperature of the carbides represented but is also higher melting than most of the other materials in the

figure. Applications of ZrC include cutting tools, gas turbine engines, nuclear environments, structural hypersonic vehicle materials, and space solar propulsion[3].

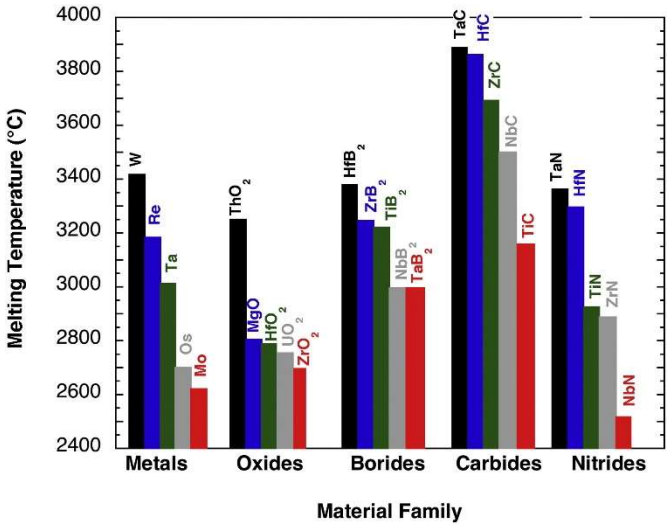

Figure 2.3: Melting temperature compared to material family, reproduced from Fahrenholtz and Hilmas[1].

2.2.2. Densification of Zirconium Carbide It is also because of this strong bonding and a low self-diffusion coefficient that ZrC tends to be difficult to sinter[69]. Elevated temperatures and pressures are typically required to densify ZrC, which can be achieved during hot pressing and spark plasma sintering (SPS)[70]. Barnier et al. produced ZrC at a relative density of 98.1% by hot pressing at 2300°C at 40 MPa for 60 mins[6], while 1 hour at 1900°C led to 96.8% relative density[69]. ZrC produced by SPS was shown to reach a relative density of 97.87% at a temperature of 1800°C and 200 MPa with a ten-minute hold[71]. Another study showed ZrC that had a relative density of 97.14% after SPS at 2100°C for 30 minutes under 80 MPa of applied pressure[72]. Reactive hot pressing can also be used to produce ZrC ceramics. Nachiappan et al. varied the molar ratios of Zr:C

during hot pressing at 40 MPa and 1200-1600°C[73]. The authors found that the stoichiometry of starting powders greatly impacts the densification of ZrC; in fact, the highest relative density of 99% was observed at 1200°C when the C/Zr ratio was 0.67.

Pressureless sintering of ZrC began in the 1970s[74] and continues to be used to densify ZrC today. Often, manipulation of starting powders and/or sintering additives must be introduced for pressureless sintering of ZrC to be successful. Schönfeld et al[10]. found that adjusting the ZrO_2:C ratio during the carbothermal reduction reaction to produce ZrC has a dramatic effect on the sinterability of ZrC. In another report, solution-based processing of ZrO_2 and C before carbothermal reduction resulted in ZrC particle sizes of 50-130 nm, which sintered to 99% relative density at 1950°C having no open porosity[75].

Molybdenum disilicide ($MoSi_2$) was used as a sintering aid with varying additions (5-20 vol%) and sintering temperatures (1850-1970°C)[70]. The highest relative density of 96.8% was achieved at a sintering temperature of 1950°C. Liquid phase sintering of composition Zr-Mo-Si-O-C was observed as well, which increased densification with increasing $MoSi_2$ content. Zhao et al. increased ZrC sinterability by particle size reduction of starting powders, adding graphite, and adding silicon carbide (SiC)[11]. High energy ball milling of as-received powders produced particles of size 0.5 μm. After sintering at 2100°C, the relative density was 98.4% with average grain sizes of 5.97 μm. Addition of graphite reduced the sintering temperature, leading to a relative density of 95.0% and grains of size 6.94 μm at 1900°C, but at 2100°C increased grain growth significantly to 15.72 μm. Finally, samples with 20 vol% SiC showed a density of 96.7%

with grains of size 3.08 μm. The addition of SiC pinned the grain boundaries, reducing intragranular porosity.

2.2.3. Microstructure, Thermal, and Mechanical Properties The microstructure of ZrC is highly dependent on the processing performed. Sintering depends on a balance between densifying and coarsening mechanisms[1]. Surface oxides present in powders can drastically increase grain growth at temperatures below the sintering temperature, limiting the final density that can be achieved[76]. Grain size, porosity, vacancies, and impurities dominate the measured values of thermal and mechanical properties that are observed in ZrC[3].

Elastic modulus of ZrC tends to fall between 380-420 GPa[4]. As a function of temperature, the elastic modulus of ZrC decreases, especially above 50% of the melting temperature when plastic deformation is more likely. As the C/Zr ratio decreases, so does elastic modulus due to a decrease in bond strength. Qian et al. calculated a theoretical elastic modulus for ZrC of 364.83 GPa[77], while Warren measured an elastic modulus of 400 GPa on a sample of $ZrC_{0.95}$ with 8% porosity[78]. Feng et al. found an elastic modulus of 404 GPa for a ZrC sample having a relative density of 96.8% and grains of 0.6 μm[69]. Another report by Landwehr et al. found an elastic modulus of 365 GPa on a sample of 98.3% relative density[7].

Ultimate fracture strength of ZrC is characterized as brittle failure. Strength measurements are highly dependent on processing history and surface/internal flaws present in measured ZrC[5]. Strength measurements are also impacted by the test method used, i.e., three-point flexural, four-point flexural, compressive, or tensile. Room temperature four-point flexural strength of near-stoichiometric ZrC was measured by

Korklan et al. to be 362 MPa with relative densities greater than 95% and a grain size of 2.7 μm[79]. The three-point flexural strength of ZrC was also measured by Lanin et al. as a function of non-isothermal sintering conditions[80]. A maximum strength of 650 MPa was reported on a sample of 92% relative density with 16 μm grains. Pressurelessly sintered ZrC with variable stoichiometry displayed a maximum strength of 309.0 MPa was recorded for a 98.9% dense sample with grains between 1.5-4.9 μm using a starting mixture of ZrO_2:C of 1:2.60[10].

Hardness of ZrC is also highly microstructure dependent and has been reported in the range of 22-34 GPa[4]. Measured hardness values are also a function of the load and tester used during testing. At a load of 0.5 kgf, the measured Vickers microhardness was 19.5 GPa and fell to 17.0 GPa at a load of 1 kgf[79]. He et al. measured Knoop hardness of ion beam-assisted deposition ZrC under a load of 10 gf to be 27.5 GPa to 30.9 varying Zr/C ratio from 0.78-0.97[81]. The authors also found that hardness increases quickly as Zr/C ratio increases from 0.5-1 but declines when Zr/C>1. Vickers microhardness on ZrC prepared by chemical vapor deposition and 98% relative density was performed at a 100 g load and found to be 27 GPa[82].

Fracture toughness of ZrC has not been widely reported but is typically seen in the range of 1.0-4.1 $MPa \cdot m^{1/2}$ [4, 7, 10, 69, 79]. Feng et al. measured fracture toughness to be 2.3 $MPa \cdot m^{1/2}$ for 96.8% dense ZrC with 0.6 μm grains[69]. Research performed by Schönfeld et al. displayed a maximum fracture toughness of 4.1 $MPa \cdot m^{1/2}$ (98.9% dense, 1.5-4.9 μm grains) and a minimum of 2.4 $MPa \cdot m^{1/2}$ (79.97% dense, 0.1-0.8 μm grains)[10]. Warren measured fracture toughness by Hertzian indentation. For ZrC of C:Zr ratio 0.95 and 8% porosity, a toughness of 1.11 $MPa \cdot m^{1/2}$ was reported.

Thermal conductivity of ZrC tends to increase with increasing temperature[5]. This behavior is attributed to both electron and phonon contributions to thermal conductivity. Grossman reports a room temperature thermal conductivity of 20.5 W/m-K[83]. The measured specimen had a relative density of 91.5% and 0.2 wt% of free carbon. The author does not quantify the grain size but mentions that there was some uniform grain growth observed. Taylor measured thermal conductivity of hot pressed ZrC on three specimens[84]. The average density was 6.16 g/cm^3 (assuming 6.73 g/cm^3 as theoretical density, this becomes 91.5% relative density) with an average grain size of 50 μm; there was at most 0.6 wt% impurity in the samples. Conductivity ranged from 31.38 W/m-K at 530°C to 43.5 W/m-K at 2100C. In another study, ZrC thermal conductivity from 150-1000°C increased from 30.6-37.3 W/m-K[85]. This sample demonstrated 98.3% relative density. Wei et al. demonstrated the heavy reliance of thermal conductivity on density[8]. At room temperature, a sample of 73.91% relative density displayed a thermal conductivity of 13.4 W/m-K while a 93.3% relative density sample had a conductivity of 30.2 W/m-K.

Electrical resistivity of ZrC can range between 60-200 μΩ cm as a function of impurities and microstructure, where increasing ZrC stoichiometry decreases resistivity[4]. Conduction electrons are scattered when there are more carbon vacancies present. Modine et al. measured room temperature resistivity of a $ZrC_{0.89}$ single crystal to be 204 μΩ cm[86], while another room temperature measurement on a single crystal of $ZrC_{0.93}$ found a resistivity of 193 μΩ cm[87], showing that even a small adjustment in the C/Zr ratio can impact the measured electrical resistivity. Room temperature resistivity measured by

Taylor on a sample of 91% relative density with 50 μm grain size was 66 μΩ cm; another sample of 92% relative density displayed a resistivity of 64 μΩ cm[84].

2.3. COLLOIDAL PROCESSING OF CERAMICS

"Colloid" is often used to define a particle of a particular size range, specifically 10^{-3}-1 μm[88]. Colloidal processing has been coined as the ability to control the interparticle forces within a suspension of ceramic powders in a medium[89]. The advantage of colloidal processing is that high and uniform particle packing can be achieved as compared to dry pressing powder[90]. Interparticle forces are the driving factor of what will make a suspension stable [88], i.e., when the suspension microstructure is homogeneous. Controlling these forces allows for a suspension to be weakly/strongly flocculated (interparticle forces are attractive) and dispersed (interparticle forces are repellant). The electrical double layer forms when a particle acquires a charge to retain electroneutrality after submersion in solution[89, 91]. This layer is composed of counterions or bound charges and arises due to the protonation/deprotonation of the ceramic surface; this reaction can be seen in Equation (1). The thickness of the electrical double layer impacts how repulsive particles may be. The forward and reverse of these reactions are controlled by the pH of the suspension. The point of zero charge (PZC) is the pH where [MOH] is equal to [MOH_2^+]. When pH is lower than pH_{PZC}, the surface charge will be positive and vice versa.

$$\begin{aligned} MOH &\leftrightarrow MO^- + H^+ \\ MOH_2^+ &\leftrightarrow MOH + H^+ \end{aligned} \qquad (1)$$

At pH_{PZC}, there are no forces other than van der Waals affecting the particles. van der Waals forces are attractive between ceramic particles, and therefore will cause flocculation in the suspension. Full homogeneous dispersion is generally the desired behavior of a suspension, as floccs, density gradients, or separation may present as a flaw in the final ceramic part.

There are three ways to disperse particles in suspension, those being steric stabilization, electrostatic stabilization, and electrosteric stabilization[88, 89]. Steric stabilization occurs when an adsorbed polymer on the surface of a colloid physically repels other colloids away from itself[92] and can be used in aqueous and non-aqueous suspensions. Electrostatic stabilization is used aqueous solutions and occurs when polyelectrolytes adsorb onto the surface of an oppositely charged particle, creating a layer of like charge between particles[93]. Finally, electrosteric stabilization utilizes both steric and electrostatic mechanisms to stabilize a suspension[94]. Polyelectrolytes used in this type of stabilization have at least one ionizable group that adsorb onto the surface of the ceramic.

Some common dispersants used in ceramic colloidal processing are Darvan 821A, Dolapix CE 64, and stearic acid. Darvan 821A is an ammonium polyacrylate that is categorized as an electrosteric dispersant and polyelectrolyte. The molecules are negatively charged, and when attached to particles, repel each other[95]. Rueschohoff et al. used this dispersant to stabilize alumina suspensions for use in direct ink write additive manufacturing[60]. Dolapix CE 64 is another example of a polyelectrolyte, except it is carbonic acid based. Rao et al. used Dolapix CE 64 to stabilize zirconia suspensions. They found that there is an electrostatic interaction between the positively charged

particle surface and the negatively charged functional groups[96] which leads to suspension stability. Stearic acid is a surfactant that was used by Li et al. to stabilize SiC feedstocks for material extrusion[97].

For this work, the anionic surfactant sodium dodecyl sulfate (SDS) is used as the dispersing species. Its molecular formula is $NaSO_4C_{12}H_{25}$. A 2D structure can be seen in Figure 2.4. The polar group is hydrophilic while the carbon chain is hydrophobic[98]. It ionizes when introduced into water, leaving the negatively charged sulfate and carbon chain to attach to the surface of the ceramic. Steric forces promote suspension stability.

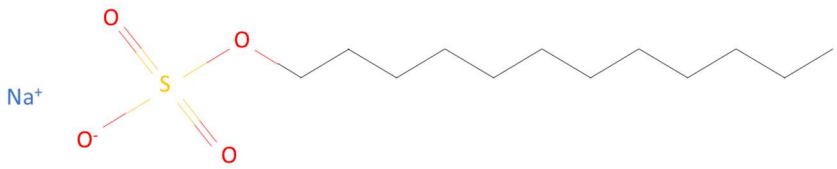

Figure 2.4: SDS chemical structure.

2.4. RHEOLOGY & MATERIAL EXTRUSION

A discussion of rheology as it relates to extrusion freeform fabrication (EFF) of ceramic pastes follows below.

A typical paste (or ink) used in EFF is classified as thixotropic[14], meaning that the viscosity of the fluid is dependent on the shear stress applied to it. These pastes are also viscoelastic, in that they behave both elastically and viscously when deformed. Pseudoplasticity refers to a material whose viscosity decreases in the presence of stress; this is also known as shear-thinning behavior[88]. These properties allow for greater material control of the feedstock that is being printed; in fact, typical polymers (such as

polylactic acid) used in fused deposition modeling (FDM), exhibit this pseudoplastic/viscoelastic behavior[99, 100].

A Herschel-Bulkley fluid is a fluid whose viscosity is too high to flow below a particular stress, namely the yield stress[62]; this is the stress at which a fluid changes behavior from elastic to viscous; the point at which this occurs is dependent on the particle network present within the fluid[88]. Equation (2) shows the Herschel-Bulkley model that describes how these fluids behave, where τ is the applied shear stress, τ_0 is the yield stress, γ is the shear rate, n is the flow behavior index (degree to which the fluid is shear thinning/thickening), and K is the consistency coefficient[101]. This model relates the shear strain a fluid may experience under the application of shear stress. In the context of EFF, minimizing both K and n can be advantageous as it allows for the necessary extrusion pressure to remain low; however, τ_0 should be high to promote shape retention post-deposition.

$$\tau = \tau_0 + K\gamma^n \tag{2}$$

The exact rheology of a paste for use in EFF is not standardized; in fact, the rheological behavior may change depending on the material system, geometrical complexity of the print, and printing parameters used[55]. For dense, complex parts, a highly loaded feedstock with a lower yield stress may be beneficial to allow the rasters to consolidate. Gap-spanning structures may benefit by using a more elastic/high yield stress feedstock to support the gap-span.

The yield stress represents an essential metric of determining how successful a feedstock may be during the printing process. There are many models that attempt to equate the yield stress to parameters such as maximum build height[102, 103]. Rau et al. put

together a "rheology roadmap," which can be used to predict the behavior of a direct ink write ink during printing[104]. The roadmap attempts to define a material's "printability." There is no set definition of the term printability, but here, the authors define printability by three main subsections: extrusion, solidification, and layer support. The extrusion subsection determines if an ink will extrude when exposed to shear stress; solidification refers to the ability of the ink to prevent spreading of the freshly deposited material; finally, layer support refers to the ability of an ink to support its own weight under the stress imposed by subsequent layers. These subsections can be used to predict if an ink will be successful during direct ink write.

During extrusion through a nozzle, a feedstock will experience a "three zone flow profile," where the material adjacent to the wall of the nozzle forms a slip plan. The yielded zone occurs next to the slip layer; this is the highest shear imparted on the paste, and so will aid in consolidating the rasters. The third layer is the inner core, which remains mostly solid, thereby promoting shape retention[105].

Common binding agents used in ceramic direct ink write include Aquazol 50, polyvinyl alcohol, and polyvinylpyrrolidone. Aquazol 50 was used in the freeze-form extrusion of alumina as reported by Huang et al[58]. It is a binding agent that does not affect the pH of a solution but increases the viscosity of an extrudate. Liu et al. utilized polyvinyl alcohol as a binder in a silicon nitride suspension[49]. Rueschhoff et al. found that polyvinylpyrrolidone is an effective binder for direct ink write of aqueous alumina pastes[60]. They found that by varying the concentration of binder, the rheological properties of the paste could be tailored as well as the mechanical strength of green bodies. All these binders work in largely the same way; the binder acts as a thickening

agent for the suspension and by varying the concentration of the binder the yield stress and viscosity of the paste can be controlled.

For this work, hydroxypropyl methylcellulose (HPMC) is used as a binding/thickening agent. HPMC has the molecular formula $C_{56}H_{108}O_{30}$. Its 2D structure can be seen in Figure 2.5. HPMC forms a gel when heated in aqueous solution. As temperature and/or time increases, the water molecules detach from the HPMC, and a hydrophobic interaction occurs between the polymer chains (cross-linking) which increases the rigidity of the solution[106, 107]. The viscosity increase can be controlled by the concentration of HPMC added to the solution, giving fine rheological control over the suspension. This effect also temporarily "locks" the suspension microstructure in place.

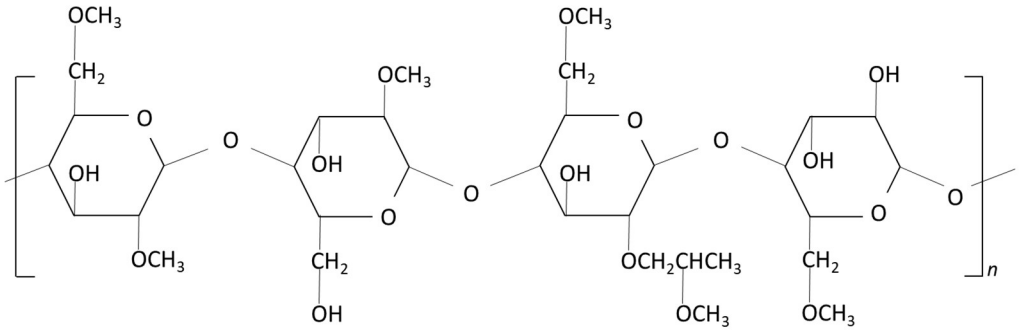

Figure 2.5: HPMC chemical structure.

PAPER

I. DEVELOPMENT OF A HIGHLY LOADED ZIRCONIUM CARBIDE PASTE FOR MATERIAL EXTRUSION ADDITIVE MANUFACTURING

Clare Sabata, Austin J. Martin, Jeremy L. Watts, Gregory E. Hilmas

Department of Materials Science and Engineering, Missouri University of Science and Technology, Rolla, MO 65409

ABSTRACT

A highly loaded, aqueous-based zirconium carbide (ZrC) paste was designed and developed for material extrusion additive manufacturing. Commercial ZrC powder was ball milled to reduce the particle size to ~1 μm. Optimal dispersant, binder, and solids loading were determined by rheological characterization and observation of the printing behavior using a paste composition consisting of 46-47 vol% ZrC, 43.5 vol% distilled water, 8.1 vol% dispersant, and 1.6 vol% binder. Rheological characterization of the paste showed a yield stress of ~8 Pa and shear thinning behavior ($\Delta G'/\Delta\sigma^* = -55$). Printing of the paste was performed using a 610 μm nozzle and a test print showed shape fidelity using the developed paste. Thermogravimetric analysis (TGA) was employed to develop a debinding schedule for unfired samples, and a pressureless sintering study was performed. Samples were debound and sintered without difficulty. A sintering temperature of 2000°C with a 2-hour hold produced samples of 90% relative density with 3.8 μm grains, which was consistent with the literature for ZrC ceramics processed by traditional routes. This temperature promoted densification while reducing grain growth

as compared to higher temperatures and hold times. The developed paste, in combination with the pressureless densification results, adds a new, ultra-high temperature material to the material extrusion method of additive manufacturing.

1. INTRODUCTION

Zirconium carbide (ZrC) is a member of the ultra-high temperature ceramics (UHTC) class of materials as it has a melting temperature of over 3000°C (~3500°C) and excellent property retention at high temperature[1]. Its high hardness (~25 GPa), elastic modulus (~400 GPa), thermal conductivity (~20 W/m-K), high wear resistance, and low density (6.73 g/cm^3) make ZrC an attractive material for applications in high-speed tooling, leading edges of hypersonic vehicles, and nuclear reactors[2–5]. Traditional processing of ZrC generally consists of powder compacts subjected to high temperatures (>2000°C) and pressures (30-100 MPa) and post-machining to obtain the desired ceramic[6]. This machining can be costly and time consuming, often accounting for up to 80% of final part costs[7, 8]. For this reason, additive manufacturing (AM) has gained popularity due to the ability to produce complex, large, and near full density parts[9].

AM of ZrC has seen success in selective laser reaction sintering (SLRS)[10] and binder jetting[11] methods. However, disadvantages exist in these techniques. SLRS resulted in cracking in the final parts due to residual stresses, while binder jetting produced parts that were only 60% of relative density. Direct ink write (DIW) is a method of AM that extrudes material layer by layer and is capable of producing large, geometrically complex, dense ceramics[9]. Ceramic pastes are extruded according to a

computer-generated shape file to effectively additively manufacture ceramic parts that can then be dried, debound, and sintered. DIW depends on the rheological behavior and drying of the ink to hold its shape once deposited[12]. Ceramic on-demand extrusion (CODE) is a method of DIW that incorporates extrusion of a highly loaded (>45 vol%) ceramic paste to build a ceramic part at room temperature that can be sintered to near full density[13]. CODE employs a dispensing system that is controlled by an auger for enhanced start/stop control of the paste during extrusion[14]. Pastes are produced with relatively low (<10 vol%) organic content, allowing for debinding that can be completed in one day or less, as compared to other ceramic extrusion methods that may take upwards of a week or more for binder burnout[15].

The fidelity of CODE printed parts depends on the rheological behavior of the paste as well as the drying of the paste post-extrusion to retain the part shape after deposition[16]. The yield stress, or where the paste begins to plastically deform, needs to be low enough for the paste to be extruded through the nozzle, while the yield stress must also recover or increase over time to support the weight of subsequent layers. Drying of the paste after deposition increases the yield stress and helps to support the structure. These behaviors begin to describe the concept of "printability," although one overall definition has not been standardized [17–19]. Controlling and characterizing the rheological behavior of pastes used in CODE aids in the development of a paste with consistent and repeatable behavior during printing.

Due to the low self-diffusion and rapid grain growth of ZrC, which often leads to intragranular porosity, it can be difficult to reach full density without the addition of external pressure[20–22]. Therefore, hot pressing (HP) or spark plasma sintering (SPS)

methods are typically required to consolidate ZrC[23–26]. These methods limit the geometries that can be produced due to the added pressure on the unfired part. As green bodies prepared from AM are near-net shape, adding non-uniform pressure to the body can deform or collapse the desired structure. Hot isostatic pressing (HIP) could be a viable method for consolidation of parts produced by AM, but at the temperatures required to process these materials, HIP becomes uneconomical[27]. Pressureless sintering, or sintering at high temperatures without added pressure, allows for near-net shape ceramics to be processed while maintaining the geometrical complexity of the printed part. However, pressurelessly sintered ZrC parts can exhibit low relative densities (<90%)[28], without the additional driving force of pressure for densification. Sintering additives and/or milling of powders are often used to increase the densification behavior of ZrC. Zhao et al.[22] showed that milling the starting ZrC powders to less than 0.5 μm leads to a density of 98.4% at 2100°C. The driving force for densification is increased when surface energy related to the particle size is high, i.e., when the particles are small[29]. This research outlines the development and characterization of a ZrC paste for use in CODE with controllable printing behavior, as well as a pressureless densification study of ZrC prepared via colloidal processing.

2. MATERIAL AND METHODS

2.1. POWDER PROCESSING

A low solids (<10 vol%) mixture of commercially available ZrC (GRADE B, d_{50}: 3-5 μm; Höganäs; Höganäs, Skane Lan, Sweden) and acetone with a 9.3:1 ratio by

weight of ¼" tungsten carbide (WC) media to ZrC was ball milled at 100 rpm until a d_{50} particle size of ~1 micron was achieved (typically 42 hours). The intensity particle size distribution of the ZrC slurry was checked at the 24-hour mark and 42-hour mark by dynamic light scattering (DLS; Litesizer 500; Anton Paar; Graz, Austria). The powder was then dried by rotary evaporation (Buchi Rotovapor R-124; BUCHI Corporation; Delaware, US) and passed through a #60 sieve (250 μm openings) to break up large aggregates. Surface area of the milled powder was determined by nitrogen adsorption analysis according to Brunauer-Emmett-Teller (BET; Nova 600; Anton Paar; Graz, Austria), and was 4.45 m^2/g on average. WC contamination was calculated by tracking the mass of milling media before and after milling and was less than 2 vol%.

2.2. PASTE DEVELOPMENT & RHEOLOGY

ZrC solids loading in the paste needs to be high enough to promote densification of the unfired part but remain low enough to avoid shear thickening behavior. Several pastes were prepared from 43 vol% to 48 vol% and their extrusion, or "printability", was characterized qualitatively during printing (e.g., slumping of paste post-deposition or paste not flowing to fill gaps) in comparison to their densification behavior. The combination of high densification and the ability to hold shape after shear was chosen as the ideal solids loading in the paste. Binder content was determined empirically. Three pastes were prepared at different levels of binder content. A low binder paste (0.02 vol%) and a high binder paste (4.3 vol%) were prepared to understand the extremes. Another paste at an intermediate binder content (1.4 vol%) was prepared, as prior work[14, 30, 31] showed that 1.4 vol% binder was effective at producing the desired rheological behavior,

i.e., sedimentation was not experienced over the time scale in which the paste was being used.

Previous aqueous processing of ZrC showed that sodium dodecyl sulfate (SDS, Sigma-Aldrich; St. Louis, MO) was an effective dispersant for ZrC[32]. Using this knowledge, a dispersant study was performed to determine the amount of dispersant per surface area of ZrC that would be most effective. Commercial unmilled ZrC powder with a known surface area of 1.29 m^2/g (BET) was combined in an aqueous slurry with dispersant. Six samples were prepared at 0, 1, 5, 9, 15, and 25 mg of dispersant per m^2 of ZrC, all at 40 vol% solids. The samples were placed on a slow speed mill (<40 rpm) for 24 hours to promote homogenization of the slurry without drastically reducing particle size. The viscosity of each sample was measured at a constant shear rate of 10 s^{-1} using a rheometer (Kinexus Ultra+; Netzsch, Geratebau GmbH; Selb, Germany) with a cone-on-plate geometry with a 4° angle, 40 mm in diameter, and a 150 μm gap to construct a dispersant curve. The same test geometry was used to perform an oscillation amplitude sweep from 0.1 Pa to 100 Pa to model the elastic and viscous response of the paste as a function of complex shear stress.

2.3. PASTE PREPARATION

Combining the results of the previous paste development experimentation, a ZrC paste was prepared. A 40 vol% slurry was prepared using milled ZrC powders, SDS, and distilled water. A 3:1 ratio by weight of ¼" spherical WC media to ZrC powder was used for milling. The media was added to an HDPE jar followed by the previously processed ceramic powder. Dispersant was added based on the surface area of ZrC present in the

batch, and finally distilled water was added. The slurry was gently shaken by hand and placed on a slow speed mill (<40 rpm) for 18-24 hours (U.S. Stoneware; East Palestine, OH, USA). A slow speed was chosen to allow homogenization of the slurry to occur while minimizing changes to the particle size of the ceramic. The slurry was then transferred to a planetary mixing jar. The required amount of cold water dispersible hydroxypropyl methylcellulose (Methocel J12MS, DOW Chemical Company; Midland, MI; USA) was calculated and added in several small additions with a 30 second, 2000 rpm planetary mix (ARE-310; THINKY Corporation; Japan) in between to ensure full distribution of the binder. Once the binder was added, binder incorporation and solvent evaporation by continuous planetary mixing commenced.

A planetary mixer (ARV-501; THINKY Corporation; Japan) equipped with a vacuum pump was utilized to reduce bubbles introduced into the paste. The paste was mixed at 1500 rpm for 180 seconds under 90 kPa vacuum several times until the paste was visually homogenous. As the paste was continuously mixed, the frictional forces within the planetary mixing jar cause the paste to heat rapidly, driving off solvent. The solvent mass loss was tracked and then used to calculate the final composition of the paste. Once the desired solids loading (46-47 vol%) was achieved, the paste was rested overnight to hydrate the binder[33] and to allow the paste to come to room temperature. The final mass loss of solvent was recorded, and the paste was loaded into a syringe barrel (Nordson EFD; Westlake, Ohio, USA) using a syringe charger (ARC-40H; THINKY Corporation; Japan).

2.4. PASTE PRINTING

A paste was prepared for CODE fabrication, following a procedure similar to Martin et. al.[16] and following the previously outlined procedures in Section 2.3. The paste was loaded into the 3-axis CODE machine and printing was performed. An applied pressure of 40 psi was utilized to force the paste through the syringe barrel nozzle and into the auger (eco-PEN300; preeflow by ViscoTec; Germany).

Full printing parameters are outlined in Table 1. The nozzle (Subrex LLC; Carlsbad, CA, USA) size was chosen as the smallest diameter the paste was able to extrude through at pressures that the system was able to sustain. The extrusion width is the width between the center of one raster to the center of the next and layer height is how much the nozzle adjusts in the Z-direction between layers. The travel speed is the rate at which the gantry moves the nozzle during paste deposition. The voltage to the auger controls how quickly the auger rotates and affects the flow rate of the paste through the nozzle. The layer dwell is adjusted depending on the size of the sample being printed and depends on the number samples being printed, where shorter times are used with large/many parts as the paste deposited at the start of that layer begins to dry while the rest of the layer/parts are being deposited. Kerosene was deposited around the edges of the print to prevent uneven drying during paste printing.

Table 1: ZrC DIW printing parameters.

Parameter	Value
Nozzle Inner Diameter	610 µm
Extrusion Width	0.61 mm
Layer Height	0.366 mm
Travel Speed	900 mm/min
Voltage to Auger	1.3 V
Layer Dwell	5 - 20 s

2.5. THERMOGRAVIMETRIC ANALYSIS & PRESSURELESS DENSIFICATION OF ZRC PASTE

Samples of green bodies, extruded and dried, were added to a thermal gravimetric analyzer (TGA; TGA-50; Shimadzu Corporation; Japan) to determine the volatilization temperatures of the organics used. A ramp rate of 10°C/min to 800°C under flowing argon gas was used. Samples of dispersant and binder were also tested under the same conditions. Based on the combination of results, a debinding schedule was created.

As introduced, the pressureless sintering of ZrC presents a challenge. Typically, high temperatures and pressures are required to produce fully dense ZrC ceramics. In order to verify the developed paste, a pressureless sintering procedure, that can produce near fully dense (≥90%) ZrC, had to be determined. Therefore, a densification study was performed. Commercial powders were processed and batched according to the previously outlined procedures in Section 2.3, and a CODE paste was prepared. Eighteen specimens were extruded into an arbitrary shape, hereafter referred to as ‘buttons’, onto a rigid polymer sheet and kerosene was wiped around the edge of the buttons to prevent uneven drying from the sides. The buttons were placed in a closed, impermeable container to promote slow solvent evaporation and dried for ~4 days. Archimedes’ principle was employed to determine the post-drying part density of the buttons by submerging four buttons in kerosene and pulling vacuum for 24 hours. The suspended and saturated masses were recorded. The buttons were then placed into a drying oven at 100°C overnight to dry and the dry mass was recorded.

The buttons were debound according to the following schedule: 1°C/min to 100°C with a one-hour hold, followed by 5°C/min ramp to 500°C for one hour with one-hour holds at 180°C, 250°C, 300°C, and 400°C, finished with a 10°C/min ramp to 600°C with

a one-hour hold under a flowing argon gas atmosphere (HTF55322A; Lindberg/Blue M; Asheville, NC, USA). For the sintering study, three temperatures (2000°C, 2050°C, and 2100°C) and two hold times (1 and 2 hours) were chosen based on prior studies in the literature[22, 34]. Three of the buttons were placed in a graphite crucible lined with graphite foil and the crucible was placed in a 4" diameter graphite furnace (1000-4560-FP30; Thermal Technology; Santa Rosa, CA, USA) equipped with a vacuum pump (TRIVAC D 16 B; Leybold GmbH; Cologne, Germany) and sintered according to the corresponding sintering schedule under flowing helium gas.

One button from each sintering schedule was sectioned via electrical discharge machining (AgieCut HSS150; GF Manufacturing Technology; Switzerland) and mounted in acrylic (VariDur; Buehler; Lake Bluff, IL, USA). The sectioned face was polished on an autopolisher (Tegramin-30; Struers; Ohio, USA) to a 0.25 μm finish using successively finer diamond abrasives for microstructural analysis by scanning electron microscopy (SEM; Axia ChemiSEM; ThermoFisher Scientific; Waltham, MA, USA).

3. RESULTS & DISCUSSION

3.1. PASTE DEVELOPMENT & RHEOLOGY

The ZrC loading was determined to be optimal with 46-47 vol% solids in the paste. This is because lower solid contents (43-45 vol%) did not hold shape during CODE printing once shear stress was removed from the paste, while 47-48 vol% solids content resulted in a paste that was too stiff to extrude through the desired nozzle size. A solids loading of 46-47 vol% also led to an unfired part density that promoted

densification during the sintering step. As for binder content, the low binder paste (0.02 vol%) exhibited low yield stress and was too fluid, causing unrecoverable slumping in the parts during printing. The high binder paste (4.3 vol%) exhibited strongly elastic behavior, trapping porosity into the part in between rasters. These respective behaviors are similar to those studied by Dudukovic et al.[35] for silica gels. The 1.4 vol% binder, 46-47 vol% ZrC paste displayed an observed balance between viscous and elastic behavior, allowing for the rasters to combine but with a high enough yield stress to hold the desired shape, similar to the intermediate volume fraction ($\varphi = 0.103$) formulations by Dudukovic et al.

The optimal dispersant concentration was found by plotting viscosity against dispersant concentration (Figure 1). The first two data points, exhibiting the highest viscosities at the lowest dispersant concentrations, indicate too little dispersant per surface area of ZrC; these high viscosities are likely due to limited steric repulsion between particles and subsequent particle agglomeration[36]. The linear increase observed in the last four data points indicates saturated or excess surface adsorption of the dispersant on the ZrC surface or dissolved in the solution; excess dispersant promotes flocculation thereby increasing viscosity. For this work, the ideal amount of dispersant was determined by where the exponential and linear curves intersect at the lowest viscosity, which was calculated to be 5.6 mg of dispersant per m^2 of ZrC.

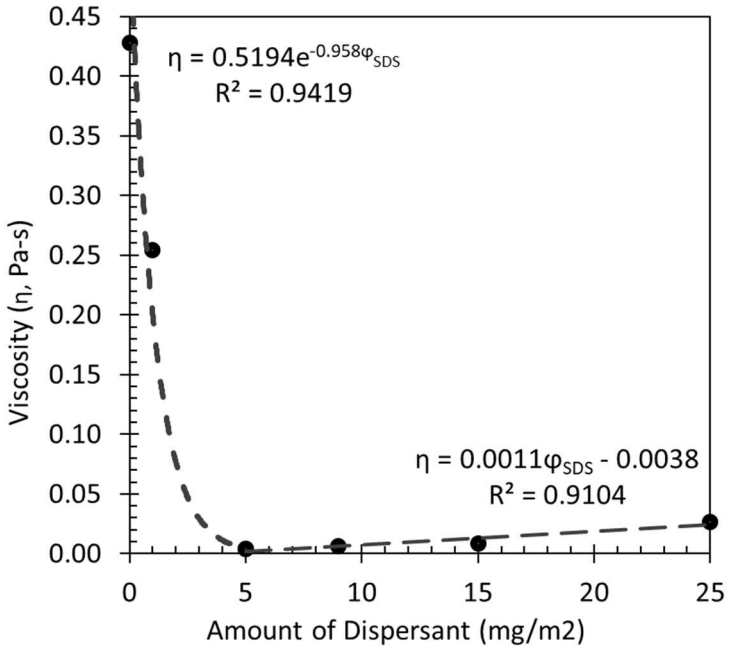

Figure 1: Viscosity versus dispersant content per m^2 of ZrC.

Combining the results from paste design, a theoretical paste composition was developed. The ideal ZrC paste composition is outlined in Table 2. While this is the ideal composition, it should be noted that the dispersant content will vary slightly based on the surface area of the powder. It should also be noted that the binder content in Table 2 is slightly higher than what was previously discussed. The 1.4 vol% binder is calculated and added on the basis of the slurry volume; therefore, after solvent evaporation and binder incorporation into the final paste, the final binder content is slightly higher.

Table 2: Ideal ZrC paste composition.

Constituent	**Volume %**	**Weight %**
Ceramic (Milled ZrC)	46-47	85-86
Solvent (Distilled Water)	43.5	11.9
Dispersant (SDS)	8.1	2.2
Binder (Methocel J12MS)	1.6	0.4

To understand the rheological behavior of the ZrC paste, an oscillation amplitude sweep was performed on CODE pastes to determine the yield and flow stresses (Figure 2). The G' curve is the elastic behavior, in-phase component, of the complex shear modulus of the paste, while the G" curve demonstrates the viscous behavior, out-of-phase component. The yield stress is where the G' curve begins to drop, or the upper limit of shear stress at which the paste begins to plastically deform. The flow stress is where the G' and G" curves crossover and represents at what shear stress the paste exhibits continual plastic deformation. The drop in G' also demonstrates shear thinning behavior as the paste behaves more liquid-like with increased stress, which allows for greater material control when 3D printing. On average, the ZrC pastes exhibited a yield stress of ~8 Pa and a flow stress of ~60 Pa. The magnitude of difference between the yield and flow stresses represents the paste transitioning quickly between "solid-like" and "liquid-like" behavior, where a smaller difference corresponds to a quicker transition. The slope ($\Delta G'/\Delta\sigma^*$) of the drop of the G' curve is -55; this "steepness" of slope relates to the sharp change between solid and liquid behavior. As the paste is extruded through a nozzle, shear stress is applied in fractions of a second. Cesarano et al. [9] found that using a paste that flows immediately when in contact with shear, but then also returns to solid-like behavior upon removal of shear, is the ideal rheological behavior. Paste behavior that transitions quickly between the two states allows for fast layer deposition and the ability of the paste to hold its shape once it has been deposited. However, depositing paste on top of a previous layer may also induce a shear stress on the paste, causing it to slump. Having a higher yield stress can prevent this; however, Lamini et al.[37] found that yield stress is highly dependent on particle size and additive content, therefore yield stress can

differ between material systems. For comparison, a typical alumina (Al_2O_3) paste that is used routinely in the CODE machine, and is very well understood and controlled[13], has a yield stress of ~17 Pa with a flow stress of ~63 Pa. These slightly higher values than what is observed in the ZrC paste can likely be attributed to the alumina paste being 13 vol% solids loading higher, leading to a slightly stiffer paste.

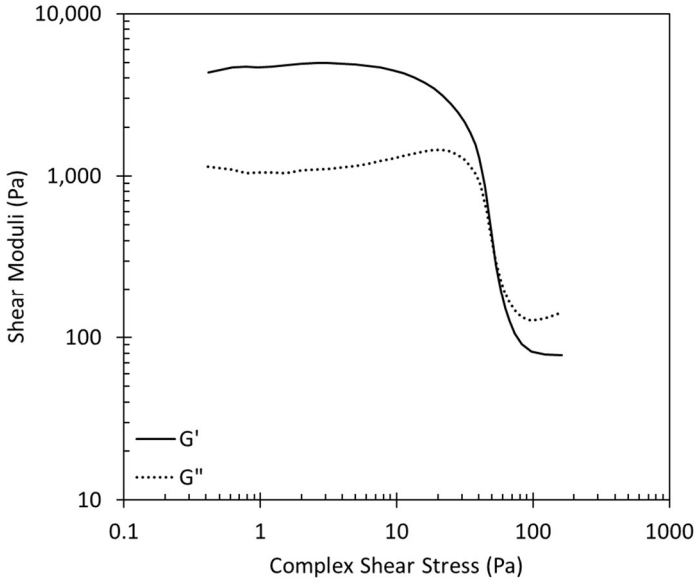

Figure 2: Shear moduli (G' and G") as a function of complex shear stress for a representative ZrC paste.

3.2. PASTE PRINTING

Following the previously outlined parameters, a 25 x 5 mm disk of fourteen layers was printed, a 3D model of which can be seen in Figure 3A. The single outer line shown on the model is the "skirt" – this is performed to prime the nozzle before printing and to ensure no clogging of the nozzle has occurred. The paste extrusion was consistent, and the print was well-defined. Figure 3B shows the disk during deposition of the third layer,

and Figure 3C shows the disk during deposition of layer thirteen. Figure 3D shows the final printed part. Visually, the extrusion is consistent, and the shape fidelity closely matches the model.

M'Barki et al.[19] proposed a relationship to link yield stress to the maximum allowable part height that can be built under the force of gravity before slumping occurs. This relationship can be seen in Equation (1) where σ_y^{Dyn} is a recovery value used by M'Barki et al.; here, the previously defined "yield stress" (Section 3.1) of 8 Pa will be used. ρ is the density of the paste calculated by a simple volumetric rule of mixtures in kg/m^3, and g is gravity of 9.81 m/s^2. Inputting these variables into Equation (1) gives a maximum part height of 0.02 cm. Clearly, this does not correspond with what can be seen in Figure 3. There is no evidence of major slumping occurring during the print. This model only accounts for the yield stress of the paste as it is still wet; after deposition, drying of the layer begins which increases yield stress. It is likely that the drying of the paste during printing allows the paste to support subsequent layers without slumping. It is also of note that M'Barki et al. applied this equation to boehmite gels, and their calculated maximum layer height did not correspond with experimental observation. Yield stress alone cannot be used to predict how a material will self-support during printing.

$$h_{max} = \frac{{\sigma_y}^{Dyn}}{\rho g} \quad (1)$$

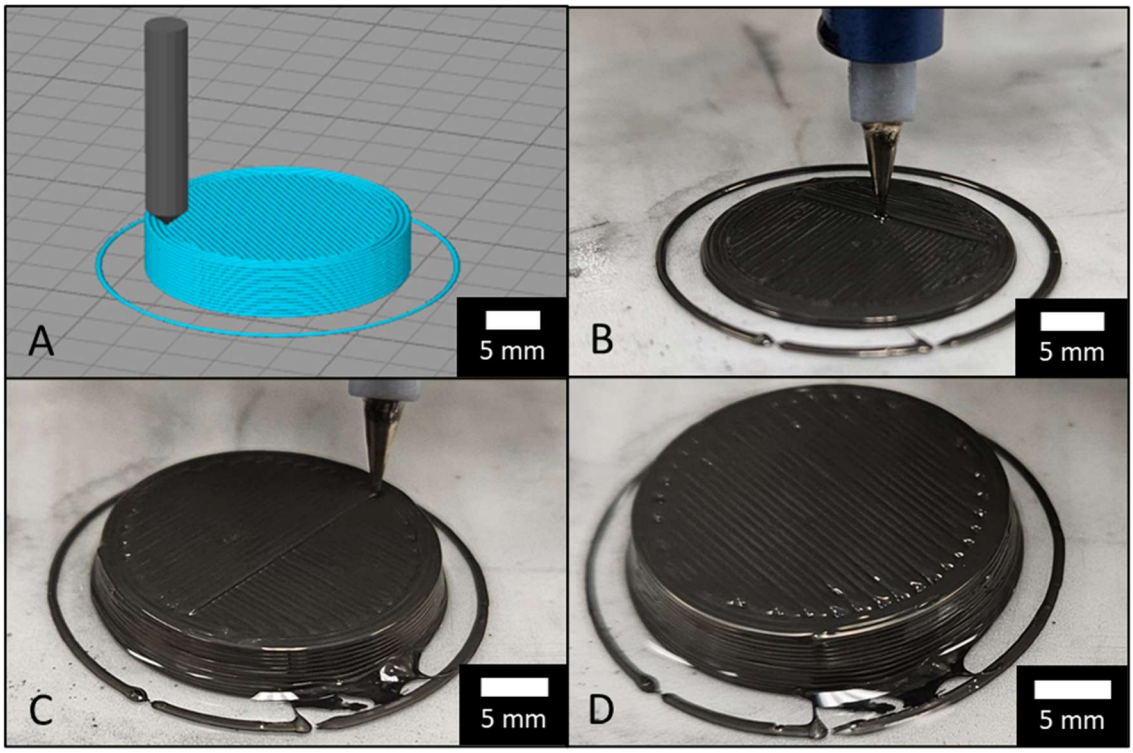

Figure 3A: 3D model of a 25 x 5 mm disk; Figure 3B: Disk during deposition of the third layer; Figure 3C: deposition of the 13th layer; Figure 3D: final printed disk. Note: the liquid seen around the bottom edge of the print is kerosene.

Roussel devised a model to determine the critical yield stress a paste must possess to form a self-supporting bead that does not spread excessively under the force of gravity[38]. This model can be seen in Equation (2), where $\sigma_{y,critical}$ is the critical yield stress (here, this will be compared to what was previously defined as "yield stress" in Section 3.2), g is gravity in m/s^2, and H is layer height in m. Using the corresponding values, the critical yield stress is 7.6 Pa compared to the measured yield stress of 8 Pa. While the measured value is close to the calculated value, it is still greater than the critical value. It may be beneficial to decrease layer height, but as excessive spreading was not observed, this may not be necessary. The layer height is limited by the nozzle diameter as it was

chosen as the smallest diameter through which the paste consistently extruded. In fact, Hu et al. [39] found a correlation between nozzle size and layer height, being that layer height should be less than 90% of the nozzle diameter. Here, the layer height was chosen to be 60% of nozzle diameter; shorter layer heights tended to drag the nozzle through the previously deposited layer. While smaller layer heights increase vertical resolution, they also increase fabrication time.

$$\sigma_{y,critical} > \frac{\rho g H}{\sqrt{3}} \tag{2}$$

3.3. THERMOGRAVIMETRIC ANALYSIS & PRESSURELESS DENSIFICATION OF ZRC PASTE

Fresh ZrC paste contained 11.9 wt% water, and the paste was determined to have lost about 12 wt% water upon drying. Therefore, the loss in mass on drying corresponded well with the water present in the paste. TGA was performed on the post-drying unfired part, as can be seen in Figure 4A. The first large drop in paste mass occurred at ~200˚C; the initial <0.5% decrease can be attributed to residual moisture in the sample evaporating. The second occurred around 400˚C. TGA was also separately performed on the dispersant and binder, as shown in Figure 4B. The dispersant showed a clear drop in mass from 200˚C to 300˚C; however, it did not decrease to zero. Therefore, it is expected that there may be some amount of sodium from the dispersant left in the microstructure prior to sintering. It is unknown if this may have a beneficial or detrimental effect on sintering. The binder shows a two-step decomposition, the first being from 250˚C to 400˚C and the second in the range of 500˚C to 600˚C. Decomposition of the binder and dispersant align with the TGA results obtained from the paste. The TGA results show a

2.5 wt% loss during decomposition of the binder and dispersant, which is roughly the same as the 2.6 wt% dispersant plus binder in the overall paste composition. Combining these results, a debinding schedule was constructed, as follows: 1˚C/min to 100˚C with a one-hour hold, followed by 5˚C/min ramp to 500˚C for one-hour with one-hour holds at 180˚C, 250˚C, 300˚C, and 400˚C, finished with a 10˚C/min ramp to 600˚C with a one-hour hold under flowing argon gas. The ramps were slow enough to prevent cracking due to rapid volatilization of water or organics with several holds to ensure full burnout of binder and dispersant.

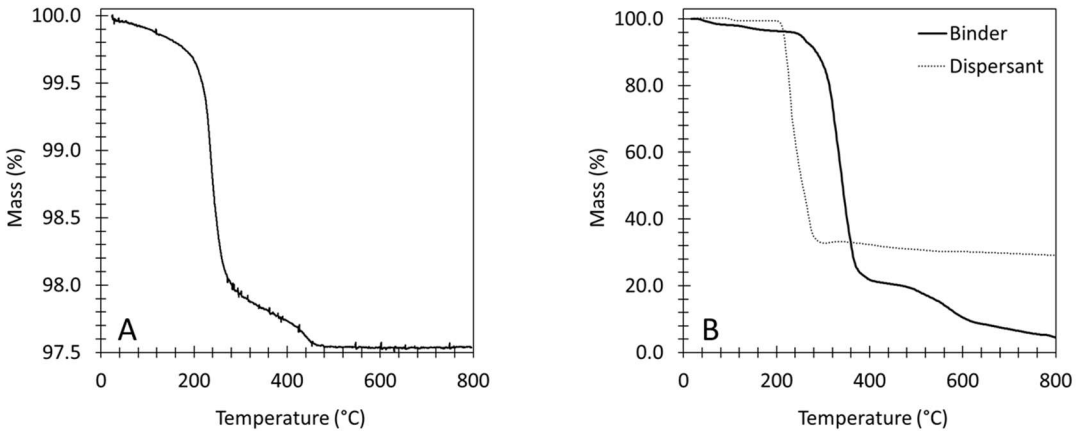

Figure 4A: Percent (%) mass versus temperature for a typical ZrC paste post-extrusion and drying. Figure 4B: Percent (%) mass versus temperature for the binder and dispersant used in a typical ZrC paste.

The unfired part density of post-drying/pre-debinding buttons was measured to be 58.4% relative density (theoretical ZrC density of 6.73 g/cm^3). The average relative densities and grain size after the pressureless paste densification study at temperatures of 2000 to 2200°C for either 1 or 2 hours can be seen in Table 3.

Table 3: Average relative densities and grain sizes for pressurelessly densified, paste-processed ZrC.

	Average Relative Density (%)	Average Grain Size (μm)	Number of Grains Counted (#)
2000°C 1 hr	85.3	2.8 ± 1.1	596
2000°C 2 hr	89.9	3.8 ± 1.4	270
2050°C 1 hr	87.0	3.5 ± 1.1	236
2050°C 2 hr	87.1	3.3 ± 1.2	723
2100°C 1 hr	90.9	4.3 ± 1.6	501
2100°C 2 hr	93.6	7.2 ± 2.8	188
2200°C 1 hr	92.6	7.8 ± 2.7	197

There is a general increase in density as temperature increases above 2050°C, with densities of 89.9% or lower at 2000 or 2050°C and densities ranging from 90.9 to 93.6% at 2100°C. Figure 5 shows a microstructure from each of the sintering schedules. The smallest grain size can be seen in the sample sintered at 2000°C for 1 hour, having a grain size of 2.8 ± 1.1 μm with minimal grain growth from the initial particle size of ~1 μm. The grains appear to exhibit necking between particles, and intragranular porosity is low as the grains did not have the ability to grow quickly enough to trap porosity. Holding at this temperature for another hour showed more grain growth and a few more instances of entrapped porosity. Increasing the temperature 50°C decreased the density slightly, from an 89.9% maximum density at 2000°C for 2 hours to ~87% dense at 2050°C for either 1 or 2 hours. It is theorized that the sintering mechanism changed somewhere between 2000°C and 2050°C, as the density decreased, and the grains began to grow rapidly past this temperature. There was a 3% increase in density between 1 and 2 hour holds at 2100°C, but grains almost doubled in size. Because of the rapid grain growth, intragranular porosity is much more prevalent. The trend continued at 2200°C for 1 hour. The grains were larger (7.8 μm) and intragranular porosity was high (Figure 5),

which likely contributed to the slight decrease in density. It was decided that 2000°C for 2 hours was the optimal sintering schedule as the density was high (~90%) while limiting grain size (3.8 ± 1.4 μm), and entrapped porosity compared to higher temperatures and hold times. In comparison, Schönfeld et al.[34] achieved 86% relative density and 0.5-2.2 μm grains at the same temperature while Zhao et al.[22] achieved a relative density of 98.4% and grains of size 5.97 μm, but at 2100°C. More work is needed to fully understand the pressureless densification behavior of ZrC, particularly for ZrC parts produced via an additive manufacturing process such as CODE.

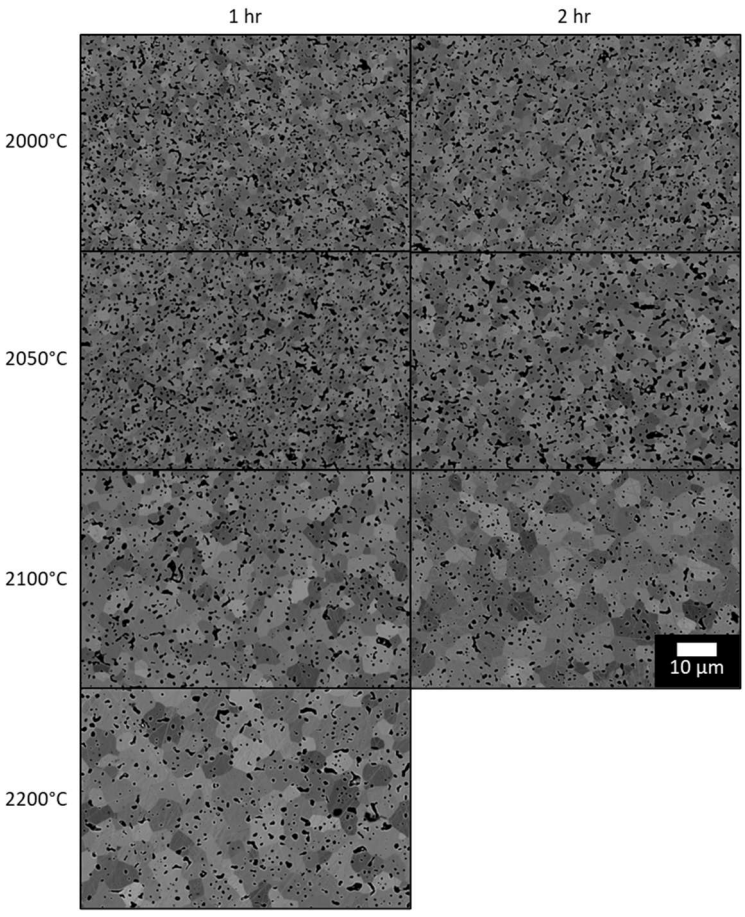

Figure 5: Representative microstructures from each of the sintering schedules.

4. CONCLUSIONS

The design and development of a ZrC paste for use in ceramic on-demand extrusion (CODE) was presented. Highly loaded (46.5 vol%) ceramic pastes were prepared with optimal dispersant (5.6 g/m^2) and binder contents (1.4 vol%). Comminution of commercial powders was employed to promote densification during sintering. Printing of the developed paste showed shape fidelity and acceptable extrusion. TGA was performed on green bodies of 58% relative density to build a debinding schedule that can be completed in a day or less. A pressureless sintering study was performed on ZrC from pastes produced in the study to determine an optimal sintering schedule of 2000°C with a 2 hour hold in flowing helium. This resulted in additively manufactured ZrC ceramics with a 90% relative density having a small grain size (~3.8 μm). The paste displayed a yield stress (~8 Pa) that was comparable to other pastes used in the CODE process (~17 Pa), and the ability to retain shape upon removal of shear stress. Future work includes characterizing the thermal and mechanical properties of ZrC prepared via CODE. The developed paste adds a new, ultra-high temperature material system to the CODE and DIW processes.

REFERENCES

1. Jackson HF, Lee WE. Properties and Characteristics of ZrC. *Comprehensive Nuclear Materials: Volume 1-5*. 2012;1–5:339–372. https://doi.org/10.1016/B978-0-08-056033-5.00023-9

2. Feng L, Fahrenholtz WG, Hilmas GE, Watts J, Zhou Y. Densification, microstructure, and mechanical properties of ZrC–SiC ceramics. *Journal of the American Ceramic Society*. 2019;102(10):5786–5795. https://doi.org/10.1111/JACE.16505

3. Wuchina E, Opila E, Opeka M, Fahrenholtz W, Talmy I. UHTCs: Ultra-High Temperature Ceramic materials for extreme environment applications. *Electrochemical Society Interface*. 2007;16(4):30–36. https://doi.org/10.1149/2.F04074IF/XML

4. Katoh Y, Vasudevamurthy G, Nozawa T, Snead LL. Properties of zirconium carbide for nuclear fuel applications. *Journal of Nuclear Materials*. 2013;441(1–3):718–742. https://doi.org/10.1016/J.JNUCMAT.2013.05.037

5. Ul-Hamid A. Microstructure, properties and applications of Zr-carbide, Zr-nitride and Zr-carbonitride coatings: a review. *Mater Adv*. 2020;1(5):1012–1037. https://doi.org/10.1039/D0MA00233J

6. Harrison RW, Lee WE. Processing and properties of ZrC, ZrN and ZrCN ceramics: a review. *Advances in Applied Ceramics*. 2016;115(5):294–307. https://doi.org/10.1179/1743676115Y.0000000061

7. Klocke F. Modern approaches for the production of ceramic components. *J Eur Ceram Soc*. 1997;17(2–3):457–465. https://doi.org/10.1016/S0955-2219(96)00163-X

8. Travitzky N, Bonet A, Dermeik B, *et al.* Additive Manufacturing of Ceramic-Based Materials. *Adv Eng Mater*. 2014;16(6):729–754. https://doi.org/https://doi.org/10.1002/adem.201400097

9. Cesarano TIl J, Baer TA, Calvert P. Recent Developments in Freeform Fabrication of Dense Ceramics From Slurry Deposition. 1997. https://doi.org/10.15781/T2GF0NG4Z

10. Peters AB, Wang C, Zhang D, *et al.* Reactive laser synthesis of ultra-high-temperature ceramics HfC, ZrC, TiC, HfN, ZrN, and TiN for additive manufacturing. *Ceram Int*. 2023;49(7):11204–11229. https://doi.org/10.1016/J.CERAMINT.2022.11.319

11. Mireles O, Wilkerson R, Medina F, Arrieta E. Additive Manufacture of Porous Zirconium Carbide for Nuclear Thermal Propulsion In-Core Insulators. *AIAA Propulsion and Energy Forum, 2021*. 2021. https://doi.org/10.2514/6.2021-3229

12. Lewis JA, Smay JE, Stuecker J, Cesarano J. Direct Ink Writing of Three-Dimensional Ceramic Structures. *Journal of the American Ceramic Society*. 2006;89(12):3599–3609. https://doi.org/https://doi.org/10.1111/j.1551-2916.2006.01382.x

13. Ghazanfari A, Li W, Leu MC, Hilmas GE. A Novel Extrusion-Based Additive Manufacturing Process for Ceramic Parts. 2016.

14. Li W, Ghazanfari A, Leu MC, Landers RG. Extrusion-on-demand methods for high solids loading ceramic paste in freeform extrusion fabrication. *Virtual Phys Prototyp*. 2017;12(3):193–205. https://doi.org/10.1080/17452759.2017.1312735

15. Rahaman MN. Ceramic processing and sintering. 2nd ed. New York: CRC Press; 2003

16. Martin AJ, Li W, Watts J, Hilmas GE, Leu MC, Huang T. Particle migration in large cross-section ceramic on-demand extrusion components. *J Eur Ceram Soc*. 2023;43(3):1087–1097. https://doi.org/https://doi.org/10.1016/j.jeurceramsoc.2022.10.059

17. Rau DA, Bortner MJ, Williams CB. A rheology roadmap for evaluating the printability of material extrusion inks. *Addit Manuf*. 2023;75:103745. https://doi.org/10.1016/j.addma.2023.103745

18. Rau DA, Williams CB, Bortner MJ. Rheology and printability: A survey of critical relationships for direct ink write materials design. *Prog Mater Sci*. 2023;140:101188. https://doi.org/10.1016/J.PMATSCI.2023.101188

19. M'Barki A, Bocquet L, Stevenson A. Linking Rheology and Printability for Dense and Strong Ceramics by Direct Ink Writing. *Sci Rep*. 2017;7(1):6017. https://doi.org/10.1038/s41598-017-06115-0

20. Andrievskii RA, Spivak II, Chevasheva KL. Effective self-diffusion coefficients in interstitial compounds. *Soviet Powder Metallurgy and Metal Ceramics*. 1968;7(7):559–562. https://doi.org/10.1007/BF00774705/METRICS

21. Fahrenholtz WG, Hilmas GE. Ultra-high temperature ceramics: Materials for extreme environments. *Scr Mater*. 2017;129:94–99. https://doi.org/https://doi.org/10.1016/j.scriptamat.2016.10.018

22. Zhao L, Jia D, Duan X, Yang Z, Zhou Y. Pressureless sintering of ZrC-based ceramics by enhancing powder sinterability. *Int J Refract Metals Hard Mater*. 2011;29(4):516–521. https://doi.org/10.1016/J.IJRMHM.2011.03.001

23. Barnier P, Brodhag C, Thevenot F. Hot-pressing kinetics of zirconium carbide. *J Mater Sci*. 1986;21(7):2547–2552. https://doi.org/10.1007/BF01114305/METRICS

24. Landwehr SE, Hilmas GE, Fahrenholtz WG, Talmy IG, DiPietro SG. Microstructure and mechanical characterization of ZrC–Mo cermets produced by hot isostatic pressing. *Materials Science and Engineering: A*. 2008;497(1–2):79–86. https://doi.org/10.1016/J.MSEA.2008.07.017

25. Wei X, Back C, Izhvanov O, Haines C, Olevsky E. Zirconium Carbide Produced by Spark Plasma Sintering and Hot Pressing: Densification Kinetics, Grain Growth, and Thermal Properties. *Materials*. 2016;9(7):577. https://doi.org/10.3390/ma9070577

26. Antou G, Mathieu G, Trolliard G, Maître A. Spark plasma sintering of zirconium carbide and oxycarbide: Finite element modeling of current density, temperature, and stress distributions. *J Mater Res*. 2009;24(2):404–412. https://doi.org/10.1557/JMR.2009.0039

27. Bocanegra-Bernal MH. Hot isostatic pressing (HIP) technology and its applications to metals and ceramics. *J Mater Sci*. 2004;39(21):6399–6420. https://doi.org/10.1023/B:JMSC.0000044878.11441.90/METRICS

28. Bulychev VP, Andrievskii RA, Nezhevenko LB. Zirconium carbide sintering. *Porosh Metall, Akad Nauk Ukr SSR; (USSR)*. 1977;4.

29. Reed JS. Principles of Ceramic Processing. 2nd ed. New York: Wiley-Interscience; 1995

30. Ghazanfari A, Li W, Leu M, Watts J, Hilmas G. Mechanical characterization of parts produced by ceramic on-demand extrusion process. *Int J Appl Ceram Technol*. 2017;14(3):486–494. https://doi.org/https://doi.org/10.1111/ijac.12665

31. Ghazanfari A, Li W, Leu MC, Watts JL, Hilmas GE. Additive manufacturing and mechanical characterization of high density fully stabilized zirconia. *Ceram Int*. 2017;43(8):6082–6088. https://doi.org/10.1016/J.CERAMINT.2017.01.154

32. Li A. Paste development and co-sintering test of zirconium carbide and tungsten in Freeze-form Extrusion Fabrication. Missouri University of Science and Technology; Rolla; 2013

33. Sarkar N, Walker LC. Hydration—dehydration properties of methylcellulose and hydroxypropylmethylcellulose. *Carbohydr Polym*. 1995;27(3):177–185. https://doi.org/10.1016/0144-8617(95)00061-B

34. Schönfeld K, Martin HP, Michaelis A. Pressureless sintering of ZrC with variable stoichiometry. *Journal of Advanced Ceramics*. 2017;6(2):165–175. https://doi.org/10.1007/S40145-017-0229-1/METRICS

35. Dudukovic NA, Ellis ME, Foster MM, *et al.* 3D printing of void-free glass monoliths: rheological and geometric considerations. *Rheol Acta*. 2022;61(10):773–784. https://doi.org/10.1007/S00397-022-01367-8/METRICS

36. Lewis JA. Colloidal Processing of Ceramics. *Journal of the American Ceramic Society*. 2000;83(10):2341–2359. https://doi.org/10.1111/J.1151-2916.2000.TB01560.X

37. Lamnini S, Elsayed H, Lakhdar Y, Baino F, Smeacetto F, Bernardo E. Robocasting of advanced ceramics: ink optimization and protocol to predict the printing parameters - A review. *Heliyon*. 2022;8(9):e10651. https://doi.org/10.1016/J.HELIYON.2022.E10651

38. Roussel N. Rheological requirements for printable concretes. *Cem Concr Res*. 2018;112:76–85. https://doi.org/10.1016/J.CEMCONRES.2018.04.005

39. Hu F, Mikolajczyk T, Pimenov DY, Gupta MK. Extrusion-Based 3D Printing of Ceramic Pastes: Mathematical Modeling and In Situ Shaping Retention Approach. *Materials 2021, Vol 14, Page 1137*. 2021;14(5):1137. https://doi.org/10.3390/MA14051137

II. THERMAL AND MECHANICAL PROPERTIES OF ZIRCONIUM CARBIDE MANUFACTURED VIA CERAMIC ON-DEMAND EXTRUSION

Clare Sabata, Jeremy L. Watts, Gregory E. Hilmas

Department of Materials Science and Engineering, Missouri University of Science and Technology, Rolla, MO 65409

ABSTRACT

Zirconium carbide (ZrC) ceramic test parts were prepared by material extrusion additive manufacturing followed by pressureless sintering at 2000°C for two hours, achieving a relative density of 90.3%. The ZrC grains were 4.6 ± 1.8 μm on average based on SEM analysis, and x-ray diffraction confirmed that ZrC was the only significant phase present. Four-point flexural strength testing exhibited an average strength of 331.3 ± 57.1 MPa (9 bars tested) and a Young's modulus of 232.8 ± 13.1 GPa. At a load of 4.91 N, the Vickers hardness was 13.6 ± 1.0 GPa (sixteen indents) and 11.6 ± 0.5 GPa at a load of 9.81 N (ten indents). Fracture toughness by direct crack method was 2.9 ± 0.2 $MPa \cdot m^{1/2}$ and Griffith analysis confirmed the largest grains as being the critical flaw for measured strength. Thermal conductivity generally increased with temperature; room temperature thermal conductivity was 13.4 W/m·K and electrical resistivity was 122.4 ± 0.5 μΩ·cm. The electron contribution to thermal conductivity was calculated to be 29% while the phonon contribution was 71%. Many of the measured properties are consistent with literature values for traditionally manufactured ZrC ceramics. This work adds to the viability of additively manufactured ZrC by material extrusion.

1. INTRODUCTION

Zirconium carbide (ZrC) is a member of the ultra-high temperature ceramic class of materials as it has a melting temperature of over 3000°C (~3500°C). It also has a low density of 6.73 g/cm^3 when compared to materials with similar melting temperatures, high hardness of 20-30 GPa, modulus of ~400 GPa, good thermal conductivity, low neutron absorption, and good chemical and abrasion resistance[1, 2]. For these properties, ZrC is of interest for use in nuclear reactors, hypersonic vehicles, high speed tooling, and many other extreme environmental applications[2–5]. ZrC is typically processed by a carbothermal reduction of the corresponding oxide, zirconia (ZrO_2)[6], followed by densification using high temperatures (>2000°C) and pressures (30-100 MPa)[7–10]. This processing greatly limits the final part geometry that is possible, as many complex shapes will collapse when subjected to high pressures in the green state. While pressureless sintering of ZrC is possible, it is difficult to reach full densification due to the rapid grain growth of ZrC, entrapping porosity into the final microstructure[11, 12]. However, when the necessary steps are taken (such as sintering additives, particle size reduction, reduction of surface oxides), densification of ZrC can be achieved by pressureless sintering [11, 13, 14].

The ability to manufacture dense, complex geometries increases the application of ZrC to many systems. However, it is costly and time consuming to machine sintered ZrC, often requiring diamond tooling[15]. Green body machining is possible, but there is no standard process for green machining of ceramics[16]. For these reasons, additive manufacturing (AM) is an attractive method of ceramic processing. Ceramic additive manufacturing has seen several successes using many methods, including binder jetting[17–20], stereolithography[21–26], and material extrusion[27–31]. As for ZrC, the only

methods currently available in literature are selective laser sintering[32], binder jetting[33], and newly, direct ink write [Sabata et al. Submitted to the *Journal of Additive Manufacturing*]. Sabata et al. developed a paste for direct ink write (DIW) with repeatable printing behavior and showed its viability. This method of DIW is known as ceramic on-demand extrusion (CODE). It uses an auger for better start/stop control of the paste during deposition, is performed at room temperature, and is aqueous based[27, 34, 35]. CODE can additively manufacture dense, complex ceramics with large cross sections (tens of centimeters).

This work characterizes several mechanical and thermal properties of ZrC parts prepared by CODE. The shrinkage and microstructure are discussed as well as results from x-ray diffraction. Four-point flexural strength, elastic modulus, hardness, and fracture toughness are reported. Thermal properties include low and high temperature thermal conductivity and low temperature electrical resistivity. This work expands upon the application of ZrC to direct ink write additive manufacturing.

2. EXPERIMENTAL PROCEDURE

2.1. SAMPLE PREPARATION

ZrC suspensions (pastes) were prepared consisting of milled commercially available ZrC powder (GRADE B, d_{50}: 3-5 μm; Höganäs; Höganäs, Skane Lan, Sweden) with a mean particle size of 1.68 μm (d_{50}; Litesizer 500; Anton Paar; Graz, Austria) and an average surface area of 4.45 m^2/g by the Brunauer-Emmett-Teller method (BET; Nova 600 Physisorption Analyzer; Anton Paar; Graz, Austria). The ZrC powder was milled

with tungsten carbide media (WC); WC contamination was tracked by measuring the mass of media before and after milling and was found to be less than 2 vol%. Pastes were prepared to 46-47 vol% ZrC content. Full paste preparation and post-processing details can be found in [Sabata et al. Submitted to the *Journal of Additive Manufacturing*].

A syringe charger (ARC-40H; THINKY Corporation; Japan) was used to load the paste into a syringe barrel (Nordson EFD; Westlake, Ohio, USA). The syringe barrel was attached to the auger (eco-PEN300; preeflow by ViscoTec; Germany) and connected to the 3-axis CODE machine. An applied pressure of 40 psi to the barrel was used to force the paste into the auger. Printing parameters were as follows: a nozzle (Subrex LLC; Carlsbad, CA, USA) inner diameter of 610 μm, extrusion width of 0.61 mm, layer height of 0.366 mm, travel speed of 900 mm/min, and layer dwell between 5-20 seconds, depending on the size of the part being printed. A voltage of 1.3 V was applied to the auger. Kerosene oil was manually deposited around the edges of the prints every three layers to reduce uneven solvent evaporation. File preparation occurred using Simplify3D (Version 4.1.0), a commercially available fused deposition modeling (FDM) slicing software followed by a custom Python script to translate the FDM file (.gcode) to a file that the CODE machine can read (.ngc). Printing of the desired geometry was executed according to the prepared file.

Post-printing, the samples were placed in a closed, impermeable container for ~4 days to slowly evaporate solvent during drying. The samples were debinded according to the following schedule: 1°C/min ramp to 100°C with a one-hour hold, followed by 5°C/min ramp to 500°C for one hour with one-hour holds at 180°C, 250°C, 300°C, and 400°C, finished with a 10°C/min ramp to 600°C with a one-hour hold under flowing

argon gas atmosphere (HTF55322A; Lindberg/Blue M; Asheville, NC, USA). Post-debinding, the samples were placed in a graphite crucible lined with graphite foil and sintered at a 20°C/min ramp to 2000°C with a two-hour hold in flowing helium atmosphere in a 4” diameter graphite furnace (1000-4560-FP30; Thermal Technology; Santa Rosa, CA, USA).

Microstructural images were obtained by scanning electron microscopy (SEM; Axia ChemiSEM; ThermoFisher Scientific; Waltham, MA, USA). Grain and pore size analysis was performed using image processing software (ImageJ; National Institutes of Health, Bethesda, MD, USA) on 663 grains from SEM micrographs. X-ray diffraction (XRD; X’Pert Pro; PANalytical; Almelo, Netherlands) was performed on a printed sample to verify phases present.

2.2. PROPERTIES TESTING

Sintered samples were mounted on a stainless-steel plate using mounting adhesive (Crystalbond; Ted Pella, Inc.; Redding, CA, USA). The surface layers were removed using a 120-grit diamond wheel (FSG-618; Chevalier Machinery; Santa Fe Springs, CA, USA). If needed, samples were cut to the necessary ASTM standard size via electrical discharge machining (AgieCut HSS150; GF Manufacturing Technology; Switzerland).

2.2.1. Mechanical Testing Four-point bend testing was conducted following ASTM C1161 to determine the flexural strength of printed ZrC parts. Samples were electrical discharge machined to roughly ASTM A-bar size (2.0 x 1.5 x 25 mm) and then surface ground with a 600-grit diamond abrasive wheel (FSG-818M; Chevalier Machinery; Santa Fe Springs, CA, USA) to the final size. The edges of the tensile surface

were manually chamfered using a 6 μm diamond pad; the tensile surfaces were polished (Tegramin-30; Struers; Ohio, USA) to a 0.25 μm finish using progressively finer diamond abrasives. A crosshead rate of 0.2 mm/min and a fully articulating A-bar test fixture (Config. A; Wyoming Test Fixtures, Inc.; Salt Lake City, UT, USA) was utilized. Strength in MPa (S) was calculated following Equation (1).

$$S = \frac{3PL}{4bd^2} \tag{1}$$

Here, P is failure load (N), L is the support span (mm), b is the specimen width (mm), and d is the specimen thickness (mm). Static Young's modulus was measured using a linear variable differential transducer positioned at the center of the test bar. Vickers microhardness (HV) was performed on the polished face of the broken bars following ASTM C1327. A load of 4.91 and 9.81 N with a 10 second press time was used, and hardness in GPa was calculated according to Equation (2) where P is the load (N) and d is the average length of the two diagonals (mm).

$$HV = 0.0018544\ (\frac{P}{d^2}) \tag{2}$$

Fracture toughness (K_{Ic}, MPa·m$^{1/2}$) was measured by the direct crack method using a Vickers hardness indenter (V-100-A2; LECO Corporation; St. Joseph, MI, USA) following the method proposed by Anstis[36] and calculated following Equation (3)(where ζ is an empirical constant equaling 0.016 ± 0.004, E is modulus of elasticity (GPa), H is hardness (GPa) at 9.81 N, P is load (N), and c is crack length (mm). An indent was made on the polished surface of the previously broken bars under a load of 98.1 N with a 15 second dwell time to propagate cracks into the sample. Using this fracture toughness, failure analysis was conducted by the Griffith criterion following ASTM C1322 to

determine the critical flaw size; the Griffith criterion is shown in Equation (4) where a is the critical flaw size, K_{Ic} is the fracture toughness (MPa·m$^{1/2}$), Y is a geometric factor related to the flaw shape, and σ is the strength (MPa).

$$K_{1c} = \zeta(\frac{E}{H})^{1/2} * \frac{P}{c^{3/2}} \quad (3)$$

$$a = (\frac{K_{1c}}{Y\sigma})^2 \quad (4)$$

2.2.2. Thermal Testing Low and high temperature thermal diffusivity was measured by the laser flash method on sample disks of size 12.6 mm x 1.98 mm following ASTM E1461. For low temperature diffusivity, the furnace ramped at a rate of 5°C/min to 200°C with three laser shots at power 1400 V and data points recorded at 30°C, 50°C, 100°C, and 200°C (Cryo2000; Anter Corp.; Pittsburgh, PA). For high temperature diffusivity, the furnace ramped at a rate of 5°C/min from 200°C to 2000°C with data points collected every 200°C using a laser power of 1400 V in flowing argon atmosphere. Both sides of the diffusivity specimens were coated with graphite spray to ensure absorption of laser light. Heat capacity was collected from the NIST-JANAF thermochemical tables[37]. Density was corrected as a function of temperature by calculating volume change from the linear thermal expansion of ZrC as reported by Touloukian[38]. Thermal conductivity was then calculated following Equation (5)(where k is the thermal conductivity in W/m·K, ρ is density in kg/m^3, d is diffusivity in m^2/s, and C_p is the heat capacity in J/kg-K.

$$k = \rho d C_p \quad (5)$$

Room temperature electrical resistivity of a printed sample was measured using the van der Pauw method[39], following ASTM F76. A disk of diameter 12.7 mm and

thickness 1.98 mm was used. Four annealed Inconel wires were placed into contact around the circumference of the disk. Three currents of 0.2, 0.3, and 0.4 A were used. The current was applied through two of the probes and the corresponding voltage was measured through the other two probes. The configuration was adjusted after each of the three currents applied for eight configurations total. The resistivity was calculated as an average of the resistivities for each current applied and the electrical conductivity was taken as the inverse of resistivity.

The Weidemann-Franz law was used to estimate the electrical contribution to thermal conductivity at room temperature[40]. The relationship is in Equation (6), where k_e is the electronic contribution to thermal conductivity (W/m·K), σ is the electrical conductivity at room temperature (S/m), L_0 is the Lorenz number, and T is the temperature (K). Typically, the Lorenz number is 2.44 x 10^{-8} W·Ω/K^2. However, as discussed in Tiwari and Feng, the Lorenz number varies as a function of temperature[41]. For the purposes of this work, a Lorenz number of 1.6 x 10^{-8} W·Ω/K^2 will be used as the room temperature value based on the discussion presented by Tiwari and Feng to reduce overprediction of the electron contribution. The phonon contribution (k_p) was determined using Equation (7), where k is thermal conductivity at room temperature.

$$k_e = \sigma L T \tag{6}$$

$$k_p = k - k_e \tag{7}$$

3. RESULTS & DISCUSSION

3.1. PRINTING

Several 56 x 7 x 6 mm bars and 25 x 5 mm disks were printed via CODE. 3D models of both geometries can be seen in Figure 1A; the single, outer line is the "skirt" and is used to prime the nozzle before printing. The paste extrusion was consistent, and the final parts closely matched the modeled shapes. Examples of the bars and a disk post-printing are displayed in Figure 1B. More printing parameters used to fabricate the bars and disks have been published elsewhere [Sabata et al. Submitted to the *Journal of Additive Manufacturing*]. There is evidence of gapping between the rasters in the top layers of the bars. This is likely due to the previously deposited paste wicking water directly out of the fresh paste, reducing the ability of the paste to flow into the gaps. This phenomenon, in combination with the quick (15 mm/s) direction changes of the printing head during deposition of the 45° infill, are likely the cause of the gapping present. For this work, these printed defects are removed via surface grinding post-sintering as they are only present in the top few layers (~5 layers = 1.8 mm). Adjustments to the Python script to slow the travel speed of the printing head around these tight corners would likely solve the issue but is currently not included in this work.

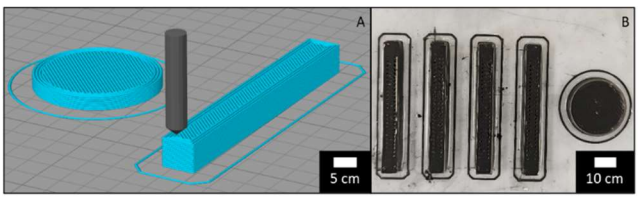

Figure 1A: 3D model of a 25 x 5 mm disk and 56 x 7 x 6 mm bar. Figure 3.1B: Several printed parts.

3.2. SHRINKAGE, MICROSTRUCTURE, AND PHASE CONTENT

Shrinkage from printed green body to printed sintered body was tracked; the samples had an average shrinkage of 11.0 ± 1.7% in both the X-Y plane and Z thickness directions. XRD was utilized to determine the phases present in the printed parts; the XRD pattern is seen in Figure 2. Based on the diffraction results, the only phase present in printed samples was ZrC.

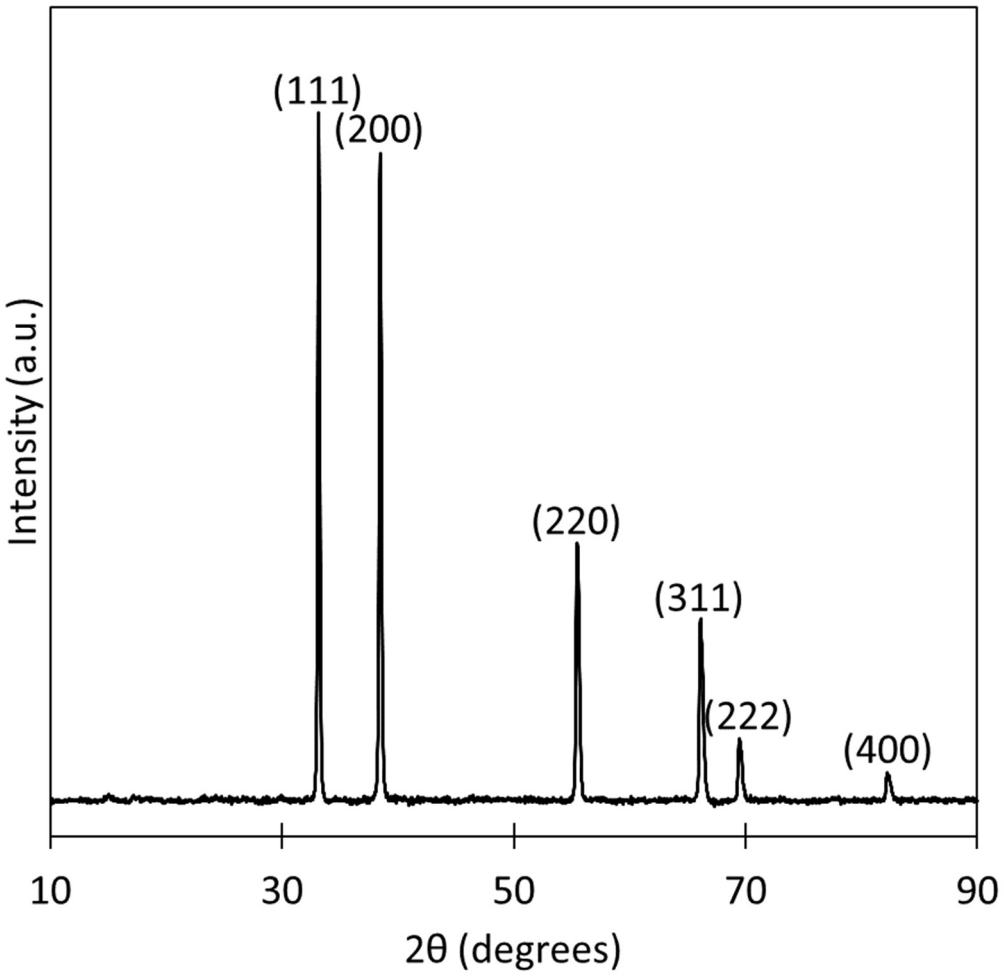

Figure 2: XRD pattern for a printed sample showing only ZrC peaks.

Figure 3 shows a representative microstructure of the printed samples. Microstructural analysis revealed a grain size of 4.6 ± 1.8 μm (663 grains counted) with a maximum grain size of 11.3 μm and an average relative density of 90.3 ± 3.0%. Further, the microstructure was consistent throughout the bulk of each sample. Porosity was also consistent (9.7%), including mostly intergranular pores and some intragranular porosity. The majority of pores (34.9%) fell within a range of 0.32-0.62 μm in size, with a maximum pore size of 7.0 μm.

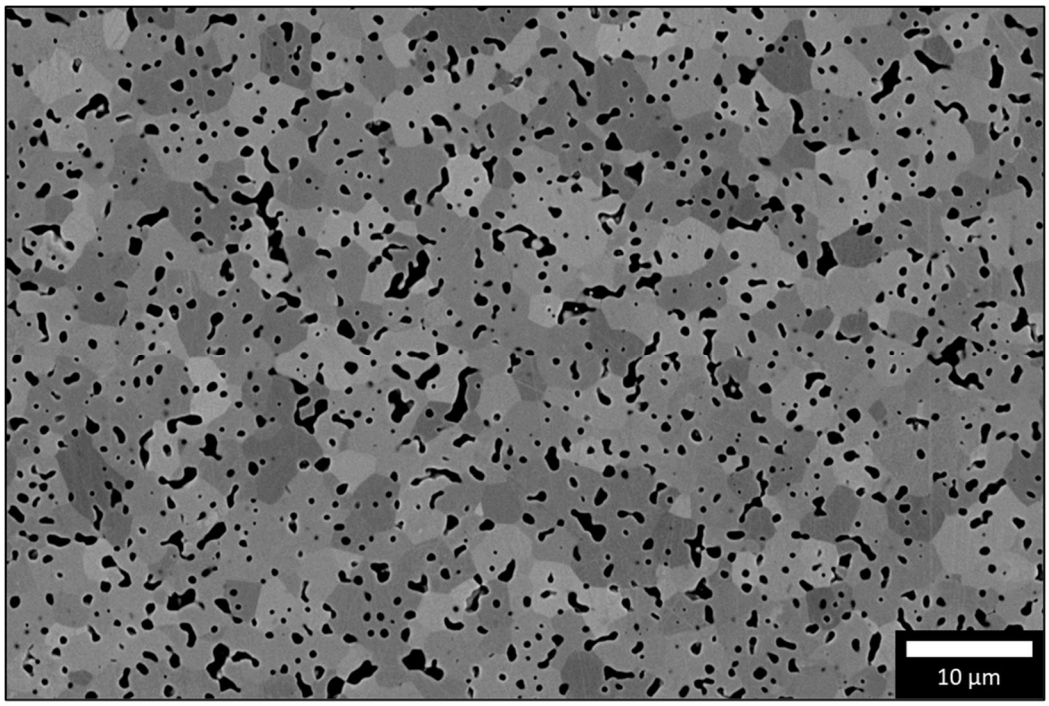

Figure 3: Microstructure of the CODE manufactured ZrC.

3.3. PROPERTIES TESTING

3.3.1. Mechanical Testing Ten ASTM "A" bars of size 2.0 x 1.5 x 25 mm were tested in four-point bend flexural testing following ASTM C1161, and final strength

values were calculated following Equation (1). One bar had a visible scratch on the tensile surface; this bar also failed at greater than two standard deviations away from the mean of the rest of the bars. Therefore, the following analysis includes the nine bars that did not contain visible surface damage. All bars broke at an average force of 101.6 N; the average strength of ZrC produced by CODE was calculated to be 331.3 ± 57.1 MPa. Traditionally processed ZrC reported in the literature have reported strength values in the range of 100-370 MPa, all of which were >95% relative density[1, 3, 13, 42]. Therefore, the measured strength values of ZrC prepared by CODE in this study are at the high end of the strengths reported in the literature. Knudsen[43] proposed a model to predict strength in relation to grain size and porosity by combining models of strength to grain size and strength to porosity. The combined model can be seen in Equation (8).

$$S = kG^{-a}e^{-bP} \tag{8}$$

Where S is the predicted strength (MPa), G is the grain size (μm), P is the volume fraction of porosity, and k, a, and b are empirical constants. Constants k, a, and b were calculated using strength, grain size, and porosity values previously published[3, 42, 44]. A systems of equations method was utilized, and k, a, and b were determined to be 330.9, -0.11, and 0.48, respectively. Calculating strength using Equation (8) with a measured grain size of 4.7 μm and volume fraction porosity of 0.097 yields a value of 374 MPa, which is 43 MPa higher than the measured value of 331.3 MPa. While the predicted value is slightly higher than the measured value, it is less than one standard deviation from the measured value; the porosity is likely not controlling the strength according to this model. Knudsen discusses that the model can be expected to predict strength to ±

10% two out of three times; therefore, while the model is a useful tool for estimating what a strength might be, it is best to take the calculated strength as an approximation.

Static Young's modulus was determined from the linear elastic portion of the flexural strength tests and determined to be 232.8 ± 13.1 GPa. Typical modulus values for ZrC fall within the range of 350-420 GPa[1, 3, 8, 45]. The low measured value is likely due to the porosity present in the samples. Nielsen[46] proposed a model to correct modulus for porosity, which can be seen in Equation (9) where E_0 is modulus adjusted for porosity (GPa), E is the measured Young's modulus (GPa), ρ is the porosity shape factor, and P is the volume fraction porosity.

$$E_0 = \frac{E(1 + (\rho^{-1} - 1)P)}{(1 - P)^2} \tag{9}$$

A Nielsen shape factor of 0.7 was selected for the calculation as some pores displayed a "ribbon" like shape while some were "pocket" shaped. Using 232.8 GPa for the measured modulus and 0.097 for the volume fraction porosity, the corrected modulus was calculated to be ~297 GPa assuming the sample was fully dense. This number is still significantly lower than what is published in the literature. However, there are two factors that can impact measured modulus by this method. The first is possible misalignment of the fixture and/or sample while the second is unaccounted compliance of the fixture or load train. Due to these factors, it is often a challenge to achieve highly accurate values for modulus by static test methods[47, 48].

Sixteen indents were measured for Vickers microhardness testing at a load of 4.91 N and ten indents were measured for a load of 9.81 N. Following ASTM C1327, Vickers hardness in GPa was calculated following Equation (2). The average hardness of ZrC

printed by CODE at a load of 4.91 N was 13.6 ± 1.0 GPa and decreased to 11.6 ± 0.5 GPa at the 9.81 N load. Slutsker et al.[49] derived a model to correct for hardness as a function of porosity for microporous silicon carbide ceramics; this model is shown in Equation (10) where H_V is the measured hardness (GPa), $H_V(0)$ is the hardness of a fully dense specimen (GPa), and P is the volume fraction of porosity. As seen in Section 3.2, the average volume fraction of porosity of parts produced via CODE is 0.097. Solving for $H_V(0)$ at both the low and high loads gives hardness values corrected for porosity of 28 and 24 GPa, respectively. These values are in good agreement with hardness values previously reported in the literature (22-34 GPa[1, 2, 8, 42]). This wide range of hardness values can be expected as hardness is heavily reliant on grain size[50], density[51], and testing load and residual stresses[52]. It is not unexpected that the decrease in hardness values observed in this study for ZrC manufactured by CODE is controlled by porosity.

$$H_V(0) \approx \frac{H_V}{(1-(1.35P)^{\frac{1}{3}})} \tag{10}$$

Fracture toughness was measured by the direct crack method. Measured Young's modulus, hardness, and crack lengths were used to estimate fracture toughness. The average fracture toughness for printed ZrC was 2.9 ± 0.2 MPa·m$^{1/2}$. However, it is important to note that there is experimental error associated with the measured values. Fracture toughness values for ZrC have been reported to be in the range of 1.0-4.1 MPa·m$^{1/2}$ from several sources[1, 3, 8, 13, 42]. A Griffith analysis using the fracture toughness of 2.9 MPa·m$^{1/2}$ noted above, and a crack geometry constant of 1.59 for a surface flaw in the shape of a semiellipse, resulted in a calculated critical flaw size of 16.6 μm. As stated earlier, most of the pores were in the range of 0.32-0.62 μm in size, with the largest pore

being 7.0 μm. Further, the average grain size was 4.6 μm. However, the largest grains measured were on the order of 11 μm which agrees with the calculated critical flaw size. Therefore, the likely critical flaw in this microstructure is the largest grain. Work performed by Korklan et al. also found the largest grain in hot-pressed ZrC as the critical flaw; Rice also compiled several reports of the largest grains in various monolithic ceramics as the strength limiting factor[42, 53]. As the grains tend to be larger than the pores, and grain growth occurs rapidly in ZrC, increasing density of the samples may not increase strength of the ceramic.

3.3.2. Thermal Testing Thermal diffusivity was measured by the laser flash method on one disk-shaped sample of size 12.7 x 1.98 mm from room temperature to 2000°C, and thermal conductivity was calculated following Equation (5). The calculated thermal conductivity as a function of temperature is reported in Figure 4. There is a sharp increase in conductivity to 17.6 W/m·K at 600°C from 12.0 W/m·K at room temperature, after which the conductivity precipitously decreased to 14.3 W/m·K. This was followed by a gradual increase in conductivity up to 24.3 W/m·K at 2000°C. While it is currently unknown why this behavior is occurring, a similar trend can be seen in previous studies in ZrC-based ceramics by Taylor[54], Landwehr et al.[55], and Grossman[56]. Jackson and Lee plotted ZrC conductivity as a function of temperature from several reported datasets and found a general increase in conductivity at low temperatures with a slight decrease at intermediate temperatures and then a gradual increase again to the melting temperature[1].

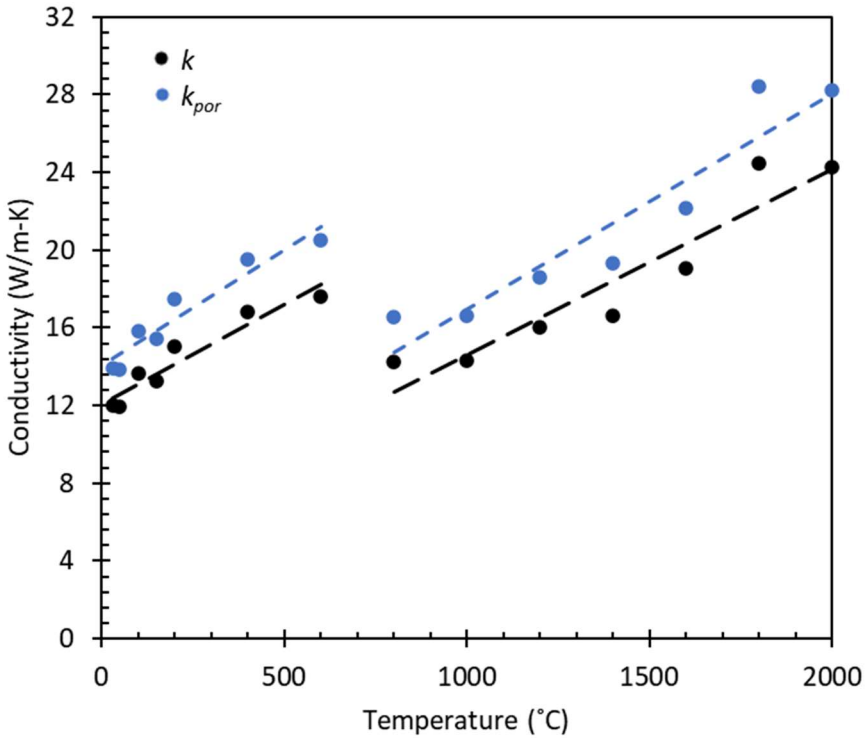

Figure 4: Printed ZrC conductivity as a function of temperature; the black line is the calculated conductivity from measured thermal diffusivity, and the blue line is conductivity adjusted for porosity present in the sample.

Thermal conductivity was adjusted for 9.7% porosity present in the samples and calculated following the Maxwell equation where k_{por} is the corrected conductivity (W/m·K), k is the measured conductivity (W/m·K), and P is the volume fraction of porosity, seen in Equation (11). The k_{por} values can also be seen in Figure 4 as the blue line. There is a 16% increase in conductivity at each temperature when adjusted for porosity present in the sample. ZrC manufactured by spark plasma sintering by Wei et al. showed a generally higher conductivity for samples of around the same density, ranging from 28 W/m·K at room temperature to 34 W/m·K at 1100°C[9].

$$k_{por} = k\frac{1 + 0.5P}{1 - P} \quad (11)$$

Room temperature electrical resistivity was measured by the van der Pauw method. The average resistivity of ZrC produced via CODE, averaging from three currents of 0.2, 0.3, and 0.4 A, was 122.4 ± 0.5 μΩ·cm. Modine et al. measured the electrical resistivity of single crystal ZrC at room temperature to be 204.2 ± 3.5 μΩ·cm[57]. Another study of single crystal resistivity was measured to be 192 μΩ·cm[58]. However, electrical resistivity of ZrC has been measured to be as low as 50 μΩ·cm and as high as 500 μΩ·cm[57, 59]. Maxwell proposed a relationship for the dependence of electrical conductivity as a function of porosity, seen in Equation (12) where σ_{th} is the conductivity of a fully dense specimen in S/m, σ is the measured conductivity in S/m, and P is the volume fraction porosity[60]. Converting the measured resistivity of 122.4 μΩ·cm to electrical conductivity results in 8.2 x 10^5 S/m. Calculating σ_{th} using the calculated conductivity and 9.7 vol% porosity gives an adjusted conductivity of 9.5 x 10^5 S/m which converts to 105.4 μΩ·cm electrical resistivity. The resistivity adjusted for porosity is slightly lower than the measured resistivity, but electrical resistivity is affected by porosity, impurities, and microstructure[61]; of which, only porosity is accounted for in Equation (12).

$$\sigma_{th} = \frac{\sigma(2 + P)}{2(1 - P)} \quad (12)$$

Using the electrical conductivity and the room temperature thermal conductivity of 13.4 W/m·K, the electron and phonon contributions to conductivity were calculated by Equations (6) and (7). At room temperature, the electronic contribution was 29% and the phonon contribution was 71%. Tiwari and Feng predicted electron and phonon

contributions to the thermal conductivity of ZrC, calculating an electron contribution of 35% and phonon contribution of 65% at room temperature, which is in good agreement with the calculated contributions from measured data in this work[41].

4. CONCLUSIONS

It has previously been shown that ZrC can be successfully additively manufactured by the direct ink write method. This work characterized the mechanical and thermal properties of ZrC prepared by this method. ZrC produced by ceramic on-demand extrusion (CODE) had an average relative density of 90.3 ± 3.0% with grains of 4.6 ± 1.8 μm. XRD confirmed that ZrC was the only phase present in printed samples. The average strength of ASTM "A"-bars was 331.3 ± 57.1 MPa, agreeing with previously reported literature, and it was shown the porosity present (9.7%) did not have a significant effect on the measured strength. Young's modulus was found to be 232.8 ± 13.1 GPa. Hardness was 13.6 ± 1.0 GPa at a load of 4.91 N and decreased to 11.6 ± 0.5 GPa at a load of 9.81 N. While these values are low, correcting the hardness values for porosity showed good agreement with the literature, confirming the porosity to be the controlling factor for hardness. Fracture toughness was 2.9 ± 0.2 $MPa \cdot m^{1/2}$, and a Griffith analysis calculated a critical flaw size of 16.6 μm which corresponded to the largest grains present in the microstructure.

Thermal conductivity was measured from room temperature to 2000°C with values ranging from 13.4 W/m·K at room temperature to 27.1 W/m·K at 2000°C. Electrical resistivity was measured to be 122.4 ± 0.5 μΩ·cm at room temperature and

used to calculate the electron (29%) and phonon (71%) contributions, which agrees with predicted values in the literature.

5. ACKNOWLEDGEMENTS

The authors would like to acknowledge Paul M. Brune for assistance in machining test samples and the members of the Ultra High Temperature Ceramics Research Group at Missouri University of Science and Technology for assistance with equipment.

REFERENCES

1. Jackson HF, Lee WE. Properties and Characteristics of ZrC. *Comprehensive Nuclear Materials: Volume 1-5*. 2012;1–5:339–372. https://doi.org/10.1016/B978-0-08-056033-5.00023-9

2. Katoh Y, Vasudevamurthy G, Nozawa T, Snead LL. Properties of zirconium carbide for nuclear fuel applications. *Journal of Nuclear Materials*. 2013;441(1–3):718–742. https://doi.org/10.1016/J.JNUCMAT.2013.05.037

3. Feng L, Fahrenholtz WG, Hilmas GE, Watts J, Zhou Y. Densification, microstructure, and mechanical properties of ZrC–SiC ceramics. *Journal of the American Ceramic Society*. 2019;102(10):5786–5795. https://doi.org/10.1111/JACE.16505

4. Wuchina E, Opila E, Opeka M, Fahrenholtz W, Talmy I. UHTCs: Ultra-High Temperature Ceramic materials for extreme environment applications. *Electrochemical Society Interface*. 2007;16(4):30–36. https://doi.org/10.1149/2.F04074IF/XML

5. Ul-Hamid A. Microstructure, properties and applications of Zr-carbide, Zr-nitride and Zr-carbonitride coatings: a review. *Mater Adv*. 2020;1(5):1012–1037. https://doi.org/10.1039/D0MA00233J

6. Fahrenholtz WG, Hilmas GE. Ultra-high temperature ceramics: Materials for extreme environments. *Scr Mater*. 2017;129:94–99. https://doi.org/https://doi.org/10.1016/j.scriptamat.2016.10.018

7. Barnier P, Brodhag C, Thevenot F. Hot-pressing kinetics of zirconium carbide. *J Mater Sci*. 1986;21(7):2547–2552. https://doi.org/10.1007/BF01114305/METRICS

8. Landwehr SE, Hilmas GE, Fahrenholtz WG, Talmy IG, DiPietro SG. Microstructure and mechanical characterization of ZrC–Mo cermets produced by hot isostatic pressing. *Materials Science and Engineering: A*. 2008;497(1–2):79–86. https://doi.org/10.1016/J.MSEA.2008.07.017

9. Wei X, Back C, Izhvanov O, Haines C, Olevsky E. Zirconium Carbide Produced by Spark Plasma Sintering and Hot Pressing: Densification Kinetics, Grain Growth, and Thermal Properties. *Materials*. 2016;9(7):577. https://doi.org/10.3390/ma9070577

10. Antou G, Mathieu G, Trolliard G, Maître A. Spark plasma sintering of zirconium carbide and oxycarbide: Finite element modeling of current density, temperature, and stress distributions. *J Mater Res*. 2009;24(2):404–412. https://doi.org/10.1557/JMR.2009.0039

11. Zhao L, Jia D, Duan X, Yang Z, Zhou Y. Pressureless sintering of ZrC-based ceramics by enhancing powder sinterability. *Int J Refract Metals Hard Mater*. 2011;29(4):516–521. https://doi.org/10.1016/J.IJRMHM.2011.03.001

12. Bulychev VP, Andrievskii RA, Nezhevenko LB. Zirconium carbide sintering. *Porosh Metall, Akad Nauk Ukr SSR; (USSR)*. 1977;4.

13. Schönfeld K, Martin HP, Michaelis A. Pressureless sintering of ZrC with variable stoichiometry. *Journal of Advanced Ceramics*. 2017;6(2):165–175. https://doi.org/10.1007/S40145-017-0229-1/METRICS

14. Silvestroni L, Sciti D. Sintering Behavior, Microstructure, and Mechanical Properties: A Comparison among Pressureless Sintered Ultra-Refractory Carbides. *Advances in Materials Science and Engineering*. 2010;2010. https://doi.org/10.1155/2010/835018

15. Travitzky N, Bonet A, Dermeik B, *et al.* Additive Manufacturing of Ceramic-Based Materials. *Adv Eng Mater*. 2014;16(6):729–754. https://doi.org/https://doi.org/10.1002/adem.201400097

16. Klocke F. Modern approaches for the production of ceramic components. *J Eur Ceram Soc*. 1997;17(2–3):457–465. https://doi.org/10.1016/S0955-2219(96)00163-X

17. Du W, Ren X, Pei Z, Ma C. Ceramic Binder Jetting Additive Manufacturing: A Literature Review on Density. *Journal of Manufacturing Science and Engineering, Transactions of the ASME*. 2020;142(4). https://doi.org/10.1115/1.4046248/1074276

18. Snelling DA, Williams CB, Suchicital CTA, Druschitz AP. Binder jetting advanced ceramics for metal-ceramic composite structures. *International Journal of Advanced Manufacturing Technology*. 2017;92(1–4):531–545. https://doi.org/10.1007/S00170-017-0139-Y/METRICS

19. Mendoza Jimenez E, Ding D, Su L, *et al.* Parametric analysis to quantify process input influence on the printed densities of binder jetted alumina ceramics. *Addit Manuf*. 2019;30:100864. https://doi.org/10.1016/j.addma.2019.100864

20. Mariani M, Beltrami R, Brusa P, Galassi C, Ardito R, Lecis N. 3D printing of fine alumina powders by binder jetting. *J Eur Ceram Soc*. 2021;41(10):5307–5315. https://doi.org/10.1016/J.JEURCERAMSOC.2021.04.006

21. Halloran JW. Ceramic Stereolithography: Additive Manufacturing for Ceramics by Photopolymerization. *https://doi.org/101146/annurev-matsci-070115-031841*. 2016;46:19–40. https://doi.org/10.1146/ANNUREV-MATSCI-070115-031841

22. Griffith ML, Halloran JW. Freeform Fabrication of Ceramics via Stereolithography. *Journal of the American Ceramic Society*. 1996;79(10):2601–2608. https://doi.org/https://doi.org/10.1111/j.1151-2916.1996.tb09022.x

23. Xing Z, Liu W, Chen Y, Li W. Effect of plasticizer on the fabrication and properties of alumina ceramic by stereolithography-based additive manufacturing. *Ceram Int*. 2018;44(16):19939–19944. https://doi.org/10.1016/J.CERAMINT.2018.07.259

24. Chartier T, Chaput C, Doreau F, Loiseau M. Stereolithography of structural complex ceramic parts. *J Mater Sci*. 2002;37(15):3141–3147. https://doi.org/10.1023/A:1016102210277/METRICS

25. Buerkle A, Brakora KF, Sarabandi K. Fabrication of a DRA array using ceramic stereolithography. *IEEE Antennas Wirel Propag Lett*. 2006;5(1):479–482. https://doi.org/10.1109/LAWP.2006.885167

26. Bae CJ, Halloran JW. Integrally Cored Ceramic Mold Fabricated by Ceramic Stereolithography. *Int J Appl Ceram Technol*. 2011;8(6):1255–1262. https://doi.org/10.1111/J.1744-7402.2010.02568.X

27. Ghazanfari A, Li W, Leu M, Watts J, Hilmas G. Mechanical characterization of parts produced by ceramic on-demand extrusion process. *Int J Appl Ceram Technol*. 2017;14(3):486–494. https://doi.org/https://doi.org/10.1111/ijac.12665

28. Li FF, Ma NN, Chen J, *et al.* SiC ceramic mirror fabricated by additive manufacturing with material extrusion and laser cladding. *Addit Manuf*. 2022;58:102994. https://doi.org/10.1016/J.ADDMA.2022.102994

29. Martin AJ, Li W, Watts J, Hilmas GE, Leu MC, Huang T. Particle migration in large cross-section ceramic on-demand extrusion components. *J Eur Ceram Soc*. 2023;43(3):1087–1097. https://doi.org/https://doi.org/10.1016/j.jeurceramsoc.2022.10.059

30. Choudhary S, Martin A, Leu MC, Hilmas G, Watts J, Huang T. Fabrication of highly dense silicon nitride parts by ceramic on-demand extrusion process and pressureless sintering. Missouri University of Science and Technology; Rolla; 2021

31. Ghazanfari A, Li W, Leu MC, Watts JL, Hilmas GE. Additive manufacturing and mechanical characterization of high density fully stabilized zirconia. *Ceram Int*. 2017;43(8):6082–6088. https://doi.org/10.1016/J.CERAMINT.2017.01.154

32. Peters AB, Wang C, Zhang D, *et al.* Reactive laser synthesis of ultra-high-temperature ceramics HfC, ZrC, TiC, HfN, ZrN, and TiN for additive manufacturing. *Ceram Int*. 2023;49(7):11204–11229. https://doi.org/10.1016/J.CERAMINT.2022.11.319

33. Mireles O, Wilkerson R, Medina F, Arrieta E. Additive Manufacture of Porous Zirconium Carbide for Nuclear Thermal Propulsion In-Core Insulators. *AIAA Propulsion and Energy Forum, 2021*. 2021. https://doi.org/10.2514/6.2021-3229

34. Li W, Ghazanfari A, Leu MC, Landers RG. Extrusion-on-demand methods for high solids loading ceramic paste in freeform extrusion fabrication. *Virtual Phys Prototyp*. 2017;12(3):193–205. https://doi.org/10.1080/17452759.2017.1312735

35. Ghazanfari A, Li W, Leu MC, Hilmas GE. A Novel Extrusion-Based Additive Manufacturing Process for Ceramic Parts. 2016.

36. ANSTIS GR, CHANTIKUL P, LAWN BR, MARSHALL DB. A Critical Evaluation of Indentation Techniques for Measuring Fracture Toughness: I, Direct Crack Measurements. *Journal of the American Ceramic Society*. 1981;64(9):533–538. https://doi.org/https://doi.org/10.1111/j.1151-2916.1981.tb10320.x

37. Chase MW. NIST-JANAF Thermochemical Tables. 4th ed. American Institute of Physics; 1998

38. Touloukian YS, Kirby RK, Taylor ER, Lee TYR. Thermophysical Properties of Matter - the TPRC Data Series. Volume 13. Thermal Expansion - Nonmetallic Solids. 1977

39. van der Pauw LJ. A Method of Measuring Specific Resistivity and Hall Effect of Discs of Arbitrary Shape. *Philips Research Reports*. 1958;13(1):1–9.

40. Franz R, Wiedemann G. Ueber die Wärme-Leitungsfähigkeit der Metalle. *Ann Phys*. 1853;165(8):497–531. https://doi.org/10.1002/andp.18531650802

41. Tiwari J, Feng T. Intrinsic thermal conductivity of ZrC from low to ultrahigh temperatures: A critical revisit. *Phys Rev Mater*. 2023;7:65001. https://doi.org/10.1103/PhysRevMaterials.7.065001

42. Korklan N, Hilmas GE, Fahrenholtz WG. Processing and room temperature mechanical properties of a zirconium carbide ceramic. *Journal of the American Ceramic Society*. 2021;104(1):413–418. https://doi.org/https://doi.org/10.1111/jace.17442

43. Knudsen FP. Dependence of Mechanical Strength of Brittle Polycrystalline Specimens on Porosity and Grain Size. *Journal of the American Ceramic Society*. 1959;42(8):376–387. https://doi.org/https://doi.org/10.1111/j.1151-2916.1959.tb13596.x

44. Lanin AG, Marchev E V., Pritchin SA. Non-isothermal sintering parameters and their influence on the structure and properties of zirconium carbide. *Ceram Int*. 1991;17(5):301–307. https://doi.org/10.1016/0272-8842(91)90026-V

45. Lengauer W. Transition Metal Carbides, Nitrides, and Carbonitrides. *Handbook of Ceramic Hard Materials*. 2000:202–252. https://doi.org/https://doi.org/10.1002/9783527618217.ch7

46. Nielsen LF. Elasticity and Damping of Porous Materials and Impregnated Materials. *Journal of the American Ceramic Society*. 1984;67(2):93–98. https://doi.org/https://doi.org/10.1111/j.1151-2916.1984.tb09622.x

47. Wachtman JB, Cannon WR, Matthewson MJ. Mechanical Properties of Ceramics. 2nd ed. John Wiley & Sons; 2009

48. Cranmer DC, Richerson DW. Mechanical testing methodology for ceramic design and reliability. 1998;434.

49. Slutsker AI, Sinani AB, Betekhtin VI, Kadomtsev AG, Ordan'yan SS. Hardness of Microporous SiC Ceramics. *Technical Physics*. 2008;53(12):1591–1596.

50. Rice RW, Wu CC, Boichelt F. Hardness–Grain-Size Relations in Ceramics. *Journal of the American Ceramic Society*. 1994;77(10):2539–2553. https://doi.org/10.1111/J.1151-2916.1994.TB04641.X

51. Rice RW. The Porosity Dependence of Physical Properties of Materials: A Summary Review. *Key Eng Mater*. 1996;115:1–20. https://doi.org/10.4028/WWW.SCIENTIFIC.NET/KEM.115.1

52. Blau PJ, Lawn BR, American Society for Testing and Materials. Committee E-4 on Metallography., International Metallographic Society., Microindentation Hardness Testing Symposium and Workshop (1984 : Philadelphia Pa). Microindentation techniques in materials science and engineering : a symposium sponsored by ASTM Committee E-4 on Metallography and by the International Metallographic Society, Philadelphia, PA, 15-18 July 1984. 1986;303.

53. Rice RW. Fractographic Identification of Strength-Controlling Flaws and Microstructure. *Concepts, Flaws, and Fractography*. 1974;323–345. https://doi.org/10.1007/978-1-4684-2991-6_17

54. TAYLOR RE. Thermal Conductivity of Zirconium Carbide at High Temperatures. *Journal of the American Ceramic Society*. 1962;45(7):353–354. https://doi.org/10.1111/j.1151-2916.1962.tb11166.x

55. Landwehr SE, Hilmas GE, Fahrenholtz WG, Talmy IG, Wang H. Thermal properties and thermal shock resistance of liquid phase sintered ZrC–Mo cermets. *Mater Chem Phys*. 2009;115(2–3):690–695. https://doi.org/10.1016/J.MATCHEMPHYS.2009.02.012

56. GROSSMAN LN. High-Temperature Thermophysical Properties of Zirconium Carbide. *Journal of the American Ceramic Society*. 1965;48(5):236–242. https://doi.org/10.1111/j.1151-2916.1965.tb14728.x

57. Modine FA, Haywood TW, Allison CY. Optical and electrical properties of single-crystalline zirconium carbide. *Phys Rev B*. 1985;32(12):7743. https://doi.org/10.1103/PhysRevB.32.7743

58. Allison CY, Finch CB, Foegelle MD, Modine FA. Low-temperature electrical resistivity of transition-metal carbides. *Solid State Commun*. 1988;68(4):387–390. https://doi.org/10.1016/0038-1098(88)90300-6

59. L.E. Toth. Transition Metal Carbides and Multilayers. *Transition Metal Carbides and Nitrides*. 1971;(January 2010):296.

60. Maxwell JC. A Treatise on Electricity and Magnetism. 3rd ed. London: Oxford University Press; 1904

61. Harrison RW, Lee WE. Processing and properties of ZrC, ZrN and ZrCN ceramics: a review. *Advances in Applied Ceramics*. 2016;115(5):294–307. https://doi.org/10.1179/1743676115Y.0000000061

SECTION

3. CONCLUSIONS AND RECOMMENDATIONS

3.1. CONCLUSIONS

Highly loaded (46-47 vol%) ceramic pastes were prepared with optimal dispersant content (5.6 m^2/g) and binder loading (1.4 vol%). Rheological characterization of the paste displayed a yield stress of ~8 Pa which agrees with other pastes used in CODE. Extrusion during printing demonstrated good shape retention upon removal of shear stress. A pressureless densification schedule (2000°C for 2 hours in He atmosphere) produced ceramics with >90% density with small grain size (<5 μm). X-ray diffraction confirmed ZrC was the only phase present, and test samples were prepared for mechanical and thermal testing. The average flexural strength of ZrC produced by CODE was 331.3 ± 57.1 MPa, which agreed with previously reported values. A Young's modulus of 232.8 ± 13.1 GPa was measured, and hardness was found to be 13.6 ± 1.0 GPa at a load of 4.91 N which decreased to 11.6 GPa ± 0.5 GPa at a load of 9.81 N. The fracture toughness was determined to be 2.9 ± 0.2 $MPa \cdot m^{1/2}$, and Griffith analysis confirmed the largest grain to be the strength limiting flaw. Thermal conductivity ranged from 13.4 W/m·K at room temperature to 27.1 W/m·K at 2000°C. Electrical resistivity was 122.4 ± 0.5 μΩ·cm which was used to find the electron (29%) and phonon (71%) contributions to thermal conductivity. This work demonstrated the successful development of a zirconium carbide (ZrC) paste for use in ceramic on-demand extrusion (CODE) and a pressureless densification study that produced highly dense ceramics.

Mechanical and thermal testing showed many properties that are comparable to traditionally processed ZrC found in the literature.

3.2. RECOMMENDATIONS

This work focused on the development of a nominally pure ZrC paste for use in material extrusion direct ink write followed by mechanical and thermal characterization. Several recommendations are provided below to enhance the measured properties of these ceramics.

1. The maximum density achieved in this work was just over 90%. The measured properties would greatly benefit from increasing overall density. This could be done by adding a sintering aid, reducing surface oxides, or perhaps by further adjusting the sintering schedule (such as holding for a longer time).
2. Determining the carbon content of the produced ZrC would allow for greater comparison to ZrC in the literature, as ZrC can have up to 50% carbon vacancies in the lattice. It would also allow for a greater understanding of how the carbon stoichiometry affects the measured properties.
3. There may be leftover sodium in the microstructure from the dispersant. Testing to determine if and how much sodium is present would give some insight into the densification behavior. Changing dispersants to one that does not contain sodium may increase the overall density that can be achieved.
4. More samples for all tests would allow for greater statistical comparison.
5. Adjusting the Python script to slow the printer head around the tight 45° infill corners may improve the gapping between the rasters during printing.

6. As this is a high temperature material, performing the mechanical and electrical resistivity measurements at a range of temperatures would give a greater understanding of how the material would be expected to behave in potential extreme environment applications.

REFERENCES

1. Fahrenholtz WG, Hilmas GE. Ultra-high temperature ceramics: Materials for extreme environments. *Scr Mater*. 2017;129:94–99. https://doi.org/https://doi.org/10.1016/j.scriptamat.2016.10.018

2. Wuchina E, Opila E, Opeka M, Fahrenholtz W, Talmy I. UHTCs: Ultra-High Temperature Ceramic materials for extreme environment applications. *Electrochemical Society Interface*. 2007;16(4):30–36. https://doi.org/10.1149/2.F04074IF/XML

3. Wuchina EJ, Opeka M. The Group IV Carbides and Nitrides. In: Fahrenholts WG, Wuchina EJ, Lee WE, Zhou Y, eds. *Ultra-High Temperature Ceramics: Materials for Extreme Environment Applications*. The American Ceramic Society; 2014:361–390.

4. Jackson HF, Lee WE. Properties and Characteristics of ZrC. *Comprehensive Nuclear Materials: Volume 1-5*. 2012;1–5:339–372. https://doi.org/10.1016/B978-0-08-056033-5.00023-9

5. Katoh Y, Vasudevamurthy G, Nozawa T, Snead LL. Properties of zirconium carbide for nuclear fuel applications. *Journal of Nuclear Materials*. 2013;441(1–3):718–742. https://doi.org/10.1016/J.JNUCMAT.2013.05.037

6. Barnier P, Brodhag C, Thevenot F. Hot-pressing kinetics of zirconium carbide. *J Mater Sci*. 1986;21(7):2547–2552. https://doi.org/10.1007/BF01114305/METRICS

7. Landwehr SE, Hilmas GE, Fahrenholtz WG, Talmy IG, DiPietro SG. Microstructure and mechanical characterization of ZrC–Mo cermets produced by hot isostatic pressing. *Materials Science and Engineering: A*. 2008;497(1–2):79–86. https://doi.org/10.1016/J.MSEA.2008.07.017

8. Wei X, Back C, Izhvanov O, Haines C, Olevsky E. Zirconium Carbide Produced by Spark Plasma Sintering and Hot Pressing: Densification Kinetics, Grain Growth, and Thermal Properties. *Materials*. 2016;9(7):577. https://doi.org/10.3390/ma9070577

9. Antou G, Mathieu G, Trolliard G, Maître A. Spark plasma sintering of zirconium carbide and oxycarbide: Finite element modeling of current density, temperature, and stress distributions. *J Mater Res*. 2009;24(2):404–412. https://doi.org/10.1557/JMR.2009.0039

10. Schönfeld K, Martin HP, Michaelis A. Pressureless sintering of ZrC with variable stoichiometry. *Journal of Advanced Ceramics*. 2017;6(2):165–175. https://doi.org/10.1007/S40145-017-0229-1/METRICS

11. Zhao L, Jia D, Duan X, Yang Z, Zhou Y. Pressureless sintering of ZrC-based ceramics by enhancing powder sinterability. *Int J Refract Metals Hard Mater*. 2011;29(4):516–521. https://doi.org/10.1016/J.IJRMHM.2011.03.001

12. Silvestroni L, Sciti D, Kling J, Lauterbach S, Kleebe HJ. Sintering Mechanisms of Zirconium and Hafnium Carbides Doped with MoSi2. *Journal of the American Ceramic Society*. 2009;92(7):1574–1579. https://doi.org/10.1111/J.1551-2916.2009.03049.X

13. Klocke F. Modern approaches for the production of ceramic components. *J Eur Ceram Soc*. 1997;17(2–3):457–465. https://doi.org/10.1016/S0955-2219(96)00163-X

14. Travitzky N, Bonet A, Dermeik B, *et al.* Additive Manufacturing of Ceramic-Based Materials. *Adv Eng Mater*. 2014;16(6):729–754. https://doi.org/https://doi.org/10.1002/adem.201400097

15. Peters AB, Wang C, Zhang D, *et al.* Reactive laser synthesis of ultra-high-temperature ceramics HfC, ZrC, TiC, HfN, ZrN, and TiN for additive manufacturing. *Ceram Int*. 2023;49(7):11204–11229. https://doi.org/10.1016/J.CERAMINT.2022.11.319

16. Mireles O, Wilkerson R, Medina F, Arrieta E. Additive Manufacture of Porous Zirconium Carbide for Nuclear Thermal Propulsion In-Core Insulators. *AIAA Propulsion and Energy Forum, 2021*. 2021. https://doi.org/10.2514/6.2021-3229

17. Li W, Ghazanfari A, Leu MC, Landers RG. Extrusion-on-demand methods for high solids loading ceramic paste in freeform extrusion fabrication. *Virtual Phys Prototyp*. 2017;12(3):193–205. https://doi.org/10.1080/17452759.2017.1312735

18. Ghazanfari A, Li W, Leu MC, Hilmas GE. A Novel Extrusion-Based Additive Manufacturing Process for Ceramic Parts. 2016.

19. Ghazanfari A, Li W, Leu MC, Watts JL, Hilmas GE. Additive manufacturing and mechanical characterization of high density fully stabilized zirconia. *Ceram Int*. 2017;43(8):6082–6088. https://doi.org/10.1016/J.CERAMINT.2017.01.154

20. Choudhary S, Martin A, Leu MC, Hilmas G, Watts J, Huang T. Fabrication of highly dense silicon nitride parts by ceramic on-demand extrusion process and pressureless sintering. Missouri University of Science and Technology; Rolla; 2021

21. Li W, Armani A, Martin A, *et al.* Extrusion-based additive manufacturing of functionally graded ceramics. *J Eur Ceram Soc*. 2021;41(3):2049–2057. https://doi.org/10.1016/J.JEURCERAMSOC.2020.10.029

22. Martin AJ, Li W, Watts J, Hilmas GE, Leu MC, Huang T. Particle migration in large cross-section ceramic on-demand extrusion components. *J Eur Ceram Soc*. 2023;43(3):1087–1097. https://doi.org/https://doi.org/10.1016/j.jeurceramsoc.2022.10.059

23. Wohlers T, Gornet T, Mostow N, *et al.* History of Additive Manufacturing. *SSRN Electronic Journal*. 2016. https://doi.org/10.2139/SSRN.4474824

24. Du W, Ren X, Pei Z, Ma C. Ceramic Binder Jetting Additive Manufacturing: A Literature Review on Density. *Journal of Manufacturing Science and Engineering, Transactions of the ASME*. 2020;142(4). https://doi.org/10.1115/1.4046248/1074276

25. Mendoza Jimenez E, Ding D, Su L, *et al.* Parametric analysis to quantify process input influence on the printed densities of binder jetted alumina ceramics. *Addit Manuf*. 2019;30:100864. https://doi.org/10.1016/j.addma.2019.100864

26. Seitz H, Rieder W, Irsen S, Leukers B, Tille C. Three-dimensional printing of porous ceramic scaffolds for bone tissue engineering. *J Biomed Mater Res B Appl Biomater*. 2005;74B(2):782–788. https://doi.org/10.1002/JBM.B.30291

27. Zocca A, Colombo P, Gomes CM, Günster J. Additive Manufacturing of Ceramics: Issues, Potentialities, and Opportunities. *Journal of the American Ceramic Society*. 2015;98(7):1983–2001. https://doi.org/10.1111/jace.13700

28. Özkol E. Rheological Characterization of Aqueous 3Y-TZP Inks Optimized for Direct Thermal Ink-Jet Printing of Ceramic Components. *Journal of the American Ceramic Society*. 2013;96(4):1124–1130. https://doi.org/https://doi.org/10.1111/jace.12285

29. Mott M, Evans JRG. Zirconia/alumina functionally graded material made by ceramic ink jet printing. *Materials Science and Engineering: A*. 1999;271(1–2):344–352. https://doi.org/10.1016/S0921-5093(99)00266-X

30. Snelling DA, Williams CB, Suchicital CTA, Druschitz AP. Binder jetting advanced ceramics for metal-ceramic composite structures. *International Journal of Advanced Manufacturing Technology*. 2017;92(1–4):531–545. https://doi.org/10.1007/S00170-017-0139-Y/METRICS

31. Mariani M, Beltrami R, Brusa P, Galassi C, Ardito R, Lecis N. 3D printing of fine alumina powders by binder jetting. *J Eur Ceram Soc*. 2021;41(10):5307–5315. https://doi.org/10.1016/J.JEURCERAMSOC.2021.04.006

32. Gibson I, Rosen D, Stucker B, Khorasani M. Binder Jetting. *Additive Manufacturing Technologies*. 2021;237–252. https://doi.org/10.1007/978-3-030-56127-7_8/TABLES/2

33. Qian B, Shen Z. Laser sintering of ceramics. *Journal of Asian Ceramic Societies*. 2013;1(4):315–321. https://doi.org/10.1016/J.JASCER.2013.08.004

34. Slocombe A, Li L. Selective laser sintering of TiC–Al2O3 composite with self-propagating high-temperature synthesis. *J Mater Process Technol*. 2001;118(1):173–178. https://doi.org/https://doi.org/10.1016/S0924-0136(01)00905-0

35. Ahmed YMZ, Zaki ZI, Bordia RK, Besisa DHA, Amin AMM. Simultaneous synthesis and sintering of TiC/Al2O3 composite via self propagating synthesis with direct consolidation technique. *Ceram Int*. 2016;42(15):16589–16597. https://doi.org/10.1016/j.ceramint.2016.07.080

36. Friedel T, Travitzky N, Niebling F, Scheffler M, Greil P. Fabrication of polymer derived ceramic parts by selective laser curing. *J Eur Ceram Soc*. 2005;25(2):193–197. https://doi.org/https://doi.org/10.1016/j.jeurceramsoc.2004.07.017

37. Bertrand P, Bayle F, Combe C, Goeuriot P, Smurov I. Ceramic components manufacturing by selective laser sintering. *Appl Surf Sci*. 2007;254(4):989–992. https://doi.org/10.1016/J.APSUSC.2007.08.085

38. Waetjen AM, Polsakiewicz DA, Kuhl I, Telle R, Fischer H. Slurry deposition by airbrush for selective laser sintering of ceramic components. *J Eur Ceram Soc*. 2009;29(1):1–6. https://doi.org/10.1016/j.jeurceramsoc.2008.05.038

39. Kumar S. Selective Laser Sintering: A Qualitative and Objective Approach. *JOM*. 2003;55(10):43–47. https://doi.org/10.1007/S11837-003-0175-Y/METRICS

40. Halloran JW. Ceramic Stereolithography: Additive Manufacturing for Ceramics by Photopolymerization. *https://doi.org/101146/annurev-matsci-070115-031841*. 2016;46:19–40. https://doi.org/10.1146/ANNUREV-MATSCI-070115-031841

41. Zakeri S, Vippola M, Levänen E. A comprehensive review of the photopolymerization of ceramic resins used in stereolithography. *Addit Manuf*. 2020;35:101177. https://doi.org/10.1016/J.ADDMA.2020.101177

42. Lee HD, Pober RL, Calvert PD, Bowen HK. Photopolymerizable binders for ceramics. *J Mater Sci Lett*. 1986;5(1):81–83. https://doi.org/10.1007/BF01671445/METRICS

43. Chartier T, Chaput C, Doreau F, Loiseau M. Stereolithography of structural complex ceramic parts. *J Mater Sci*. 2002;37(15):3141–3147. https://doi.org/10.1023/A:1016102210277/METRICS

44. Xing Z, Liu W, Chen Y, Li W. Effect of plasticizer on the fabrication and properties of alumina ceramic by stereolithography-based additive manufacturing. *Ceram Int*. 2018;44(16):19939–19944. https://doi.org/10.1016/J.CERAMINT.2018.07.259

45. Bae CJ, Halloran JW. Integrally Cored Ceramic Mold Fabricated by Ceramic Stereolithography. *Int J Appl Ceram Technol*. 2011;8(6):1255–1262. https://doi.org/10.1111/J.1744-7402.2010.02568.X

46. Buerkle A, Brakora KF, Sarabandi K. Fabrication of a DRA array using ceramic stereolithography. *IEEE Antennas Wirel Propag Lett*. 2006;5(1):479–482. https://doi.org/10.1109/LAWP.2006.885167

47. Brakora KF, Halloran J, Sarabandi K. Design of 3-D monolithic MMW antennas using ceramic stereolithography. *IEEE Trans Antennas Propag*. 2007;55(3 II):790–797. https://doi.org/10.1109/TAP.2007.891855

48. Dermeik B, Travitzky N. Laminated Object Manufacturing of Ceramic-Based Materials. *Adv Eng Mater*. 2020;22(9):2000256. https://doi.org/10.1002/ADEM.202000256

49. Liu S, Ye F, Liu L, Liu Q. Feasibility of preparing of silicon nitride ceramics components by aqueous tape casting in combination with laminated object manufacturing. *Materials & Design (1980-2015)*. 2015;66(PA):331–335. https://doi.org/10.1016/J.MATDES.2014.10.079

50. Zhang Y, He X, Du S, Zhang J. Al2O3 Ceramics Preparation by LOM (Laminated Object Manufacturing). *The International Journal of Advanced Manufacturing Technology*. 2001;17(7):531–534. https://doi.org/10.1007/s001700170154

51. Gomes CM, Rambo CR, De Oliveira APN, *et al.* Colloidal Processing of Glass–Ceramics for Laminated Object Manufacturing. *Journal of the American Ceramic Society*. 2009;92(6):1186–1191. https://doi.org/10.1111/J.1551-2916.2009.03035.X

52. Zhang G, Chen H, Yang S, *et al.* Frozen slurry-based laminated object manufacturing to fabricate porous ceramic with oriented lamellar structure. *J Eur Ceram Soc*. 2018;38(11):4014–4019. https://doi.org/10.1016/J.JEURCERAMSOC.2018.04.032

53. Cesarano TIl J, Baer TA, Calvert P. Recent Developments in Freeform Fabrication of Dense Ceramics From Slurry Deposition. 1997. https://doi.org/10.15781/T2GF0NG4Z

54. Guo N, Leu MC. Additive manufacturing: technology, applications and research needs. *Frontiers of Mechanical Engineering 2013 8:3*. 2013;8(3):215–243. https://doi.org/10.1007/S11465-013-0248-8

55. Lamnini S, Elsayed H, Lakhdar Y, Baino F, Smeacetto F, Bernardo E. Robocasting of advanced ceramics: ink optimization and protocol to predict the printing parameters - A review. *Heliyon*. 2022;8(9):e10651. https://doi.org/10.1016/J.HELIYON.2022.E10651

56. Conzelmann NA, Gorjan L, Sarraf F, *et al.* Manufacturing complex Al2O3 ceramic structures using consumer-grade fused deposition modelling printers. *Rapid Prototyp J*. 2020;26(6):1035–1048. https://doi.org/10.1108/RPJ-05-2019-0133/FULL/XML

57. Lombardi JL, Hoffinan RA, Waters JA, Popovich D, Souvignier C. Issues Associated with EFF & FDM Ceramic Filled Feedstock Formulation. n.d.

58. Huang T, Mason MS, Hilmas GE, Leu MC. Freeze-form Extrusion Fabrication of Ceramics. 2005.

59. Hossain SS, Lu K. Recent progress of alumina ceramics by direct ink writing: Ink design, printing and post-processing. *Ceram Int*. 2023;49(7):10199–10212. https://doi.org/10.1016/J.CERAMINT.2023.01.143

60. Rueschhoff L, Costakis W, Michie M, Youngblood J, Trice R. Additive Manufacturing of Dense Ceramic Parts via Direct Ink Writing of Aqueous Alumina Suspensions. *Int J Appl Ceram Technol*. 2016;13(5):821–830. https://doi.org/10.1111/IJAC.12557

61. Glymond D, Vandeperre LJ. Robocasting of MgO-doped alumina using alginic acid slurries. *Journal of the American Ceramic Society*. 2018;101(8):3309–3316. https://doi.org/10.1111/JACE.15509

62. Shahzad A, Lazoglu I. Direct ink writing (DIW) of structural and functional ceramics: Recent achievements and future challenges. *Compos B Eng*. 2021;225:109249. https://doi.org/10.1016/J.COMPOSITESB.2021.109249

63. Cui K, Mao H, Zhang Y, *et al.* Microstructure, mechanical properties, and reinforcement mechanism of carbide toughened ZrC-based ultra-high temperature ceramics: A review. *Compos Interfaces*. 2022;29(7):729–748. https://doi.org/10.1080/09276440.2021.2012409

64. Guillermet AF. Analysis of thermochemical properties and phase stability in the zirconium-carbon system . *J Alloys Compd*. 1995;217:69–89.

65. Gasparrini C, Rana D sham, Le Brun N, *et al.* On the stoichiometry of zirconium carbide. *Scientific Reports 2020 10:1*. 2020;10(1):1–12. https://doi.org/10.1038/s41598-020-63037-0

66. Momma K, Izumi F. VESTA 3 for three-dimensional visualization of crystal, volumetric and morphology data. *J Appl Crystallogr*. 2011;44(6):1272–1276. https://doi.org/10.1107/S0021889811038970

67. Harrison RW, Lee WE. Processing and properties of ZrC, ZrN and ZrCN ceramics: a review. *Advances in Applied Ceramics*. 2016;115(5):294–307. https://doi.org/10.1179/1743676115Y.0000000061

68. Little EJ, Jones MM. A complete table of electronegativities. *J Chem Educ*. 1960;37(5):231–233. https://doi.org/10.1021/ED037P231

69. Feng L, Fahrenholtz WG, Hilmas GE, Watts J, Zhou Y. Densification, microstructure, and mechanical properties of ZrC–SiC ceramics. *Journal of the American Ceramic Society*. 2019;102(10):5786–5795. https://doi.org/10.1111/JACE.16505

70. Silvestroni L, Sciti D. Sintering Behavior, Microstructure, and Mechanical Properties: A Comparison among Pressureless Sintered Ultra-Refractory Carbides. *Advances in Materials Science and Engineering*. 2010;2010. https://doi.org/10.1155/2010/835018

71. Wei X, Back C, Izhvanov O, Khasanov OL, Haines CD, Olevsky EA. Spark Plasma Sintering of Commercial Zirconium Carbide Powders: Densification Behavior and Mechanical Properties. *Materials 2015, Vol 8, Pages 6043-6061*. 2015;8(9):6043–6061. https://doi.org/10.3390/MA8095289

72. Feng L, Lee S, Lee H. Nano-sized zirconium carbide powder: Synthesis and densification using a spark plasma sintering apparatus. *Int J Refract Metals Hard Mater*. 2017;64:98–105. https://doi.org/https://doi.org/10.1016/j.ijrmhm.2017.01.006

73. Nachiappan C, Rangaraj L, Divakar C, Jayaram V. Synthesis and densification of monolithic zirconium carbide by reactive hot pressing. *Journal of the American Ceramic Society*. 2010;93(5):1341–1346. https://doi.org/10.1111/J.1551-2916.2010.03608.X

74. Bulychev VP, Andrievskii RA, Nezhevenko LB. Zirconium carbide sintering. *Porosh Metall, Akad Nauk Ukr SSR; (USSR)*. 1977;4.

75. Sacks MD, Wang CA, Yang Z, Jain A. Carbothermal reduction synthesis of nanocrystalline zirconium carbide and hafnium carbide powders using solution-derived precursors. *J Mater Sci*. 2004;39(19):6057–6066. https://doi.org/10.1023/B:JMSC.0000041702.76858.A7/METRICS

76. Sciti D, Silvestroni L, Medri V, Monteverde F. Sintering and Densification Mechanisms of Ultra-High Temperature Ceramics. *Ultra-High Temperature Ceramics: Materials for Extreme Environment Applications*. Vol. 9781118700785. John Wiley & Sons, Ltd; 2014:112–143. https://doi.org/10.1002/9781118700853.CH6

77. QIAN J, WU C yi, GONG H ran. Phase transition, thermodynamic and elastic properties of ZrC. *Transactions of Nonferrous Metals Society of China*. 2018;28(12):2520–2527. https://doi.org/10.1016/S1003-6326(18)64898-8

78. Warren R. Measurement of the fracture properties of brittle solids by hertzian indentation. *Acta Metallurgica*. 1978;26(11):1759–1769. https://doi.org/10.1016/0001-6160(78)90087-1

79. Korklan N, Hilmas GE, Fahrenholtz WG. Processing and room temperature mechanical properties of a zirconium carbide ceramic. *Journal of the American Ceramic Society*. 2021;104(1):413–418. https://doi.org/https://doi.org/10.1111/jace.17442

80. Lanin AG, Marchev E V., Pritchin SA. Non-isothermal sintering parameters and their influence on the structure and properties of zirconium carbide. *Ceram Int*. 1991;17(5):301–307. https://doi.org/10.1016/0272-8842(91)90026-V

81. He X-M, Shu L, Li H-B, Li H-D, Lee S-T. Structural characteristics and hardness of zirconium carbide films prepared by tri-ion beam-assisted deposition. *Journal of Vacuum Science & Technology A*. 1998;16(4):2337–2344. https://doi.org/10.1116/1.581349

82. Ogawa T, Ikawa K, Iwamoto K. Microhardness and microstructure of chemically vapor deposited ZrC-C alloy. *Journal of Nuclear Materials*. 1976;62(2–3):322–324.

83. GROSSMAN LN. High-Temperature Thermophysical Properties of Zirconium Carbide. *Journal of the American Ceramic Society*. 1965;48(5):236–242. https://doi.org/10.1111/j.1151-2916.1965.tb14728.x

84. TAYLOR RE. Thermal Conductivity of Zirconium Carbide at High Temperatures. *Journal of the American Ceramic Society*. 1962;45(7):353–354. https://doi.org/10.1111/j.1151-2916.1962.tb11166.x

85. Landwehr SE, Hilmas GE, Fahrenholtz WG, Talmy IG, Wang H. Thermal properties and thermal shock resistance of liquid phase sintered ZrC–Mo cermets. *Mater Chem Phys*. 2009;115(2–3):690–695. https://doi.org/10.1016/J.MATCHEMPHYS.2009.02.012

86. Modine FA, Haywood TW, Allison CY. Optical and electrical properties of single-crystalline zirconium carbide. *Phys Rev B*. 1985;32(12):7743. https://doi.org/10.1103/PhysRevB.32.7743

87. Allison CY, Finch CB, Foegelle MD, Modine FA. Low-temperature electrical resistivity of transition-metal carbides. *Solid State Commun*. 1988;68(4):387–390. https://doi.org/10.1016/0038-1098(88)90300-6

88. Lewis JA. Colloidal Processing of Ceramics. *Journal of the American Ceramic Society*. 2000;83(10):2341–2359. https://doi.org/10.1111/J.1151-2916.2000.TB01560.X

89. Bergstrom L. Handbook of Applied Colloid and Surface Chemistry. Weinheim: Wiley; 2002

90. Tallon C, Franks G V. Near-Net-Shaping of Ultra-High Temperature Ceramics. In: Fahrenholtz WG, Wuchina EJ, Lee WE, Zhou Y, eds. *Ultra-High Temperature Ceramics: Materials for Extreme Environment Applications*. John Wiley & Sons, Ltd; 2014:83–111.

91. James RO, Parks GA. Surface and Colloid Science. Springer; 1982

92. Napper DH, Netschey A. Studies of the steric stabilization of colloidal particles. *J Colloid Interface Sci*. 1971;37(3):528–535. https://doi.org/10.1016/0021-9797(71)90330-4

93. Hierrezuelo J, Sadeghpour A, Szilagyi I, Vaccaro A, Borkovec M. Electrostatic stabilization of charged colloidal particles with adsorbed polyelectrolytes of opposite charge. *Langmuir*. 2010;26(19):15109–15111. https://doi.org/10.1021/LA102912U/SUPPL_FILE/LA102912U_SI_001.PDF

94. Fritz G, Schädler V, Willenbacher N, Wagner NJ. Electrosteric stabilization of colloidal dispersions. *Langmuir*. 2002;18(16):6381–6390. https://doi.org/10.1021/LA015734J/ASSET/IMAGES/LARGE/LA015734JF00010.JPEG

95. Cunniffe GM, O'Brien FJ, Partap S, Levingstone TJ, Stanton KT, Dickson GR. The synthesis and characterization of nanophase hydroxyapatite using a novel dispersant-aided precipitation method. *J Biomed Mater Res A*. 2010;95A(4):1142–1149. https://doi.org/10.1002/JBM.A.32931

96. Rao SP, Tripathy SS, Raichur AM. Dispersion studies of sub-micron zirconia using Dolapix CE 64. *Colloids Surf A Physicochem Eng Asp*. 2007;302(1–3):553–558. https://doi.org/10.1016/J.COLSURFA.2007.03.034

97. Li FF, Ma NN, Chen J, *et al.* SiC ceramic mirror fabricated by additive manufacturing with material extrusion and laser cladding. *Addit Manuf*. 2022;58:102994. https://doi.org/10.1016/J.ADDMA.2022.102994

98. Singer MM, Tjeerdema RS. Fate and effects of the surfactant sodium dodecyl sulfate. *Rev Environ Contam Toxicol*. 1993;133:95–149. https://doi.org/10.1007/978-1-4613-9529-4_3/COVER

99. Hamad K, Kaseem M, Deri F, Hamad K, Kaseem M, Deri F. Melt Rheology of Poly(Lactic Acid)/Low Density Polyethylene Polymer Blends. *Advances in Chemical Engineering and Science*. 2011;1(4):208–214. https://doi.org/10.4236/ACES.2011.14030

100. Fang Q, Hanna MA. Rheological properties of amorphous and semicrystalline polylactic acid polymers. *Ind Crops Prod*. 1999;10(1):47–53. https://doi.org/https://doi.org/10.1016/S0926-6690(99)00009-6

101. Herschel WH, Bulkley R. Konsistenzmessungen von Gummi-Benzollösungen. *Kolloid-Zeitschrift*. 1926;39(4):291–300. https://doi.org/10.1007/BF01432034

102. Roussel N. Rheological requirements for printable concretes. *Cem Concr Res*. 2018;112:76–85. https://doi.org/10.1016/J.CEMCONRES.2018.04.005

103. M'Barki A, Bocquet L, Stevenson A. Linking Rheology and Printability for Dense and Strong Ceramics by Direct Ink Writing. *Sci Rep*. 2017;7(1):6017. https://doi.org/10.1038/s41598-017-06115-0

104. Rau DA, Bortner MJ, Williams CB. A rheology roadmap for evaluating the printability of material extrusion inks. *Addit Manuf*. 2023;75:103745. https://doi.org/10.1016/j.addma.2023.103745

105. Smay JE, Cesarano J, Lewis JA. Colloidal Inks for Directed Assembly of 3-D Periodic Structures. *Langmuir*. 2002;18(14):5429–5437. https://doi.org/10.1021/la0257135

106. Sarkar N, Walker LC. Hydration—dehydration properties of methylcellulose and hydroxypropylmethylcellulose. *Carbohydr Polym*. 1995;27(3):177–185. https://doi.org/10.1016/0144-8617(95)00061-B

107. Stephen AM, Phillips GO, Williams PA, editors. Food Polysaccharides and Their Applications. 2nd ed. Boca Raton: Taylor & Francis Group; 2006

VITA

Clare Sabata was born in Colorado Springs, Colorado. She graduated high school from Lee's Summit North High School outside of Kansas City, Missouri. After graduating high school in 2017, she moved to Rolla, Missouri to attend the Missouri University of Science and Technology where she earned her Bachelor of Science in Ceramic Engineering in the fall of 2021.

In the spring of 2022, she began her graduate work at the Missouri University of Science and Technology. Her research focused on the additive manufacturing of advanced ceramics. Clare received her Master of Science in Ceramic Engineering from the Missouri University of Science and Technology in May of 2024.